Sustainable Energy & Fuels

ROYAL SOCIETY OF CHEMISTRY

PAPER

View Article Online
View Journal | View Issue

Check for updates

Cite this: *Sustainable Energy Fuels*, 2026, **10**, 1174

Investigation of interfacial charge-carrier dynamics, degradation, and recombination mechanisms in single-junction perovskite solar cells with NiO_x and SAM hole-transporting layers *via* steady-state drift-diffusion model simulations

Ivona Kafedjiska, *[a,d] Vincent M. Le Corre,[b] Hans Köbler,[c,d] Igal Levine,[d]
Rutger Schlatmann[a,d,e] and Iver Lauermann[a,d]

We investigate the stability and the degradation pathways in single-junction perovskite solar cells with four varying hole-transporting layers (HTLs): pure nickel oxide (NiO_x) and copper-doped (NiO_x:Cu), with or without self-assembled monolayer (SAM) surface passivation. The cells are aged in a continuous MPP-tracking set-up in a nitrogen environment at 25 °C and the *JV* curves prior to and after the aging are fitted *via* drift-diffusion simulations. By using a set of experimentally-measured input parameters and correlating the results from the experiments with the simulations, we are able to test the reliability of the model and then extract important information about the interfacial charge-carrier dynamics, recombination, and degradation mechanisms in the solar cells. We find that NiO_x induces severe electron trapping and poor band alignment at the NiO_x–perovskite interface, thereby leading to the highest quasi-Fermi level splitting to open-circuit voltage (QFLS–V_{oc}) offset among all the HTLs. As the cells age, the density of bulk traps when NiO_x, NiO_x:Cu, and NiO_x:Cu + SAM are used increases by factors of 36, 3, and 8, respectively, while for NiO_x + SAM it remains unchanged. For all of the HTLs, the non-radiative Shockley–Read–Hall (SRH) recombination *via* surface traps is the dominant recombination mechanism, as it is around 2–3 orders of magnitude higher than the direct or bulk-SRH recombination pathway. Additionally, NiO_x exhibits an around 2 orders of magnitude higher rate of SRH interfacial recombination compared to the other three HTLs. However, as the cells age, the rate of the interface SRH recombination remains relatively stable, but the bulk SRH recombination increases by an order of magnitude in all cells, indicating that the degradation of the cells is directly proportional to the increase of the trap-assisted recombination in the perovskite bulk and its degradation. Finally, we investigate the correlation between the hysteresis factor (HF) and the ion concentration. We find that the devices with NiO_x have the highest HF and the highest negative-ion concentration, in good agreement with the finding of electron trapping and the highest trap-assisted recombination rate for the NiO_x samples. Combining all of this information, we can explain why NiO_x is the least stable HTL among all the HTLs (15% loss in the initial PCE) and how its stability can be improved with Cu doping (8% loss in the initial PCE) and, to an extent, with SAM passivation (around 11% loss in the initial PCE).

Received 5th April 2025
Accepted 8th January 2026

DOI: 10.1039/d5se00474h

rsc.li/sustainable-energy

1. Introduction

Over the past ten years, perovskite-based solar cells have seen an unprecedented growth in their power-conversion efficiency. Single-junction perovskite and monolithic Si–perovskite tandem solar cells have reached PCEs of 26.2% and 34.6%, respectively.[1] Single-junction perovskite solar cells are attractive as a top-cell technology for Si. These perovskite-based tandem photovoltaics solar cells are especially attractive due to their higher PCE and therefore, the ability to generate a higher amount of electricity for a given installation area. Therefore, there is a strong incentive to industrialize this PV technology,

---

[a] *Helmholtz-Zentrum Berlin für Materialien und Energie GmbH, Competence Centre for Photovoltaics (PVcomB), Schwarzschildstraße 3, 12489 Berlin, Germany. E-mail: ivona.kafedjiska@helmholtz-berlin.de*

[b] *Mads Clausen Institute, Center for Advanced Photovoltaics and Thin Film Energy Devices (SDU CAPE), University of Southern Denmark, 6400 Sonderborg, Denmark*

[c] *Helmholtz-Zentrum Berlin für Materialien und Energie, Department Active Materials and Interfaces for Stable Perovskite Solar Cells, Albert-Einstein-Straße 16, 12489 Berlin, Germany*

[d] *Helmholtz-Zentrum Berlin für Materialien und Energie GmbH, Division Solar Energy, Kekuléstraße 5, 12489 Berlin, Germany*

[e] *Faculty 1 – Energy and Information, Hochschule für Technik und Wirtschaft Berlin, Germany*

especially for densely-populated areas where the available land for PV installations might be limited.

However, this market-oriented goal is strongly limited by the unproven long-term stability of perovskite-based PVs during outdoor operating conditions and by the significant gap in the community's understanding regarding the main degradation pathways. So far, several degradation stress parameters have been detected – including moisture, oxygen, reverse bias, heat, and light.[2] Some of these issues have been tackled by primarily altering the perovskite bulk, for instance *via* compositional engineering of the perovskite crystal or by using a mixture of 2D–3D perovskite.[3–6] In addition to the perovskite bulk, its interface to the charge-transport layers (CTLs) is just as important, as the trap-assisted recombination at the perovskite–CTL interfaces or ion migration can severely hinder the device stability.[7–11]

Recently it has been suggested that the detected hysteresis in perovskite solar cells is a direct consequence of the coupling of ion (vacancy) migration predominantly with trap-assisted interface recombination.[12–14] Both of these phenomena – ion vacancies and trap-assisted recombination – are detrimental for the cells' stability. On the one hand, some studies indicate that an increased field-screening effect caused by mobile ions and an increase in the mobile-ion densities are the dominant loss mechanism in perovskite cells, surpassing trap-assisted recombination in the bulk and at the interfaces.[15] On the other hand, other studies show that an increased electric-field screening and an increase in the density of ion vacancies are not sufficient to deteriorate the cells' stability, unless accompanied by an increase in the recombination in the perovskite bulk.[16] Finally, novel studies even indicate that mobile ions and ion vacancies can even be beneficial for the cells, as long as suitable interface passivation techniques that boost the devices' V_{oc} are implemented.[17]

One reason as to why the discussion on the predominant degradation mechanisms is still open is because the impact of the mobile ions or the trap-assisted recombination at the interfaces or in the perovskite bulk is highly dependent on the perovskite interface with the CTLs. This argument is additionally supported by the many findings that consistently show that altering the perovskite interface to the CTLs can lead to suppression of hysteresis, even when the perovskite is left unchanged. The interface is usually altered either by surface passivation[11,18] or fully exchanging one charge-transport layer for another.[15,19,20] However, hysteresis can re-appear at low temperatures when organic transport layers are used[21] or even with varying light intensity[22] and/or scan rate.[13–15]

Hole-transport layers (HTLs), their interface with the perovskite, and their impact on trap-assisted recombination have been extensively investigated. Novel studies further indicate that HTLs and their interface with the perovskite are more sensitive than electron-transport layers (ETLs) to halide vacancies, ionic field screening effects, and increased interface recombination, which consecutively lead to a loss in the PCE over time.[15] In fact, there is a plethora of materials for the HTLs, but only a modest number of widely-used ETLs. For instance, most of the tandem-compatible single-junction p-i-n (inverted) perovskite solar cells are using C_{60} and BCP or SnO_2 as the ETL stack, but the HTLs can either be organic (for instance, PTAA, Spiro-OMeTAD, or self-assembled monolayers (SAMs)) or inorganic (for instance, nickel oxide, NiO_x) materials.[23] It is often argued that organic molecules can deliver higher PCEs compared to inorganic HTLs, but that the latter are superior in their stability.[23] The only exception is possibly SAMs, which have been shown to simultaneously lead to high PCE and satisfactory stability.[24] Compared to PTAA, SAMs have also been shown to slow down ion-induced degradation losses in perovskite cells.[15] However, SAMs as stand-alone HTLs can be problematic when used on rough surfaces, such as a bottom CIGS cell or textured Si, as the monolayer cannot conformally cover the rough surface, leading to the formation of ohmic shunts in the devices.[25] Combining SAMs with an underlying oxide, such as NiO_x, copper-doped NiO_x[18,26] or indium zinc oxide (IZO),[27] can circumvent this issue.

Among all inorganic HTLs, NiO_x has been the most investigated one, mostly due to its suitable opto-electronic properties, promising stability, and low manufacturing costs.[28] However, NiO_x exhibits varying stoichiometry between NiO (Ni^{2+}) and Ni_2O_3 (Ni^{3+}) that greatly influences its performance in the devices.[28–36] Increasing the (Ni^{3+}) content often leads to conductivity enhancement, but also to loss in transparency[37–40] and stability, primarily due to Ni^{3+}-induced chemical reactions at the NiO_x–perovskite interface.[8,41] These issues can be tackled either by physically doping the NiO_x[42–46] or by passivating its surface,[47–49] and therefore, its interface to the perovskite, or by combination of both approaches.[18,26] Interface engineering usually aims to improve the energy level alignment, to passivate defects, to improve the charge-carrier dynamics, to mitigate ion migration, and even to create a barrier for moisture penetration.[50]

However, despite the many studies focusing on improving the PCE of the NiO_x-based perovskite devices, there has not been much systematic investigation of the impact of the simultaneous alteration of the NiO_x bulk and surface on the overall device stability. While extensive research has compared the stability of NiO_x to organic hole transport layers (HTLs), such as PEDOT:PSS, PTAA, Spiro-OMeTAD, or self-assembled monolayers (SAMs), our work shifts the focus toward enhancing the intrinsic performance and stability of NiO_x itself. This perspective is particularly relevant under a combination of constraints that are essential for perovskite-based tandem architectures.

Specifically, the approach presented in this paper is novel in that it employs (1) ITO substrates, (2) magnetron-sputtered NiO_x without high-temperature annealing, (3) combined bulk doping and surface passivation of NiO_x, (4) wide-bandgap triple-cation perovskite absorbers compatible with tandem architectures, (5) operational stability assessment *via* continuous maximum power point (MPP) tracking and drift-diffusion simulations, and (6) simulation-based analysis of aged devices to investigate the degradation mechanisms. Most existing studies diverge from these conditions, or cover only one or two of them at best, while the investigation of the cells' stability by simultaneous simulation of both fresh and aged cells has not yet been demonstrated.

For instance, magnetron-sputtered NiO_x is by now is a widely-used material in perovskite solar cells, but mostly in combination with high-temperature post-deposition treatments. Recently, a PCE of around 23% was achieved by surface passivation and post-annealing at 300 °C of NiO_x – the highest PCE for sputtered NiO_x.[51,52] However, the cells lost 14% from their PCE after 500 hours of continuous MPP tracking.[51] Thus, optimizing both the PCE and the stability of magnetron-sputtered NiO_x without adopting high-temperature post-treatments is extremely challenging and PCEs remain in the range of around 15%.[53] The lack of post-annealing treatments makes the as-sputtered NiO_x highly susceptible to hydroxides and Ni^{3+} species that can then potentially induce chemical reactions and degrade the NiO_x–perovskite interface.[8,41,52]

Similarly, a number of studies employ FTO substrates and solution-processed NiO_x layers that require high-temperature annealing,[54–56] limiting their compatibility with tandem integration. Moreover, many works utilize $MAPbI_3$-based perovskites,[54,55] which are also not optimal for tandem top cells due to their narrower bandgap. Stability assessments in these cases are often restricted to storage in ambient or inert atmospheres without continuous operational tracking.[47,57–59]

For example, Almora *et al.* demonstrated improved stability of NiO_x through surface passivation with various chemical treatments including HI and PbI_2.[54] However, the device architecture (FTO/NiO_x/$MAPbI_3$) and the lack of MPP tracking limit its relevance. Similarly, Mohanraj *et al.* employed PbI_2, Li-TFSI, and phenylethylamine for NiO_x passivation and tracked stability over 80 hours at MPP,[55] yet their architecture and material system remain non-tandem compatible.

Other studies focus on storage-based stability tests without illumination. Sharma *et al.* improved shelf-life using fluorinated benzoic acids, though the evaluation was limited to humid storage.[58] Zhou *et al.* used a TBT-based SAM to modify NiO_x, achieving 88.7% PCE retention after 2635 hours at 60 °C in a glovebox, but without operational stress.[57] Zhumagali *et al.* applied a ruthenium-based dye to improve interfacial stability, with devices retaining ~80% of the initial PCE after 500 hours at 85 °C, without encapsulation or continuous illumination.[47]

More rigorous thermal and operational testing was performed by Li *et al.*, who used a p-type organic semiconductor (TPA-BA) to modify NiO_x, resulting in 90% PCE retention after 1000 hours of continuous light soaking at 85 °C.[60] Similarly, Yang *et al.* improved both the performance and the stability using triazinyl modification, with operational testing under various encapsulated and unencapsulated conditions.[61] While promising, these examples still rely on solution-processed NiO_x and high-temperature annealing. Wang *et al.* presented one of the most robust demonstrations of operational stability, reporting >2000 h at 85 °C with AlO_x/SiO_x passivation layers;[56] however, their use of sol–gel NiO_x with 400 °C annealing makes their method also incompatible with temperature-sensitive tandem configurations.

Therefore, although the literature vastly highlights the benefits of surface modification and passivation of NiO_x, there remains a critical gap in understanding the degradation mechanisms in wide-bandgap perovskite solar cells with low-temperature, sputtered NiO_x compatible for tandem architectures.

Motivated by this research gap, we are focusing on systematically investigating the changes in cells' stability and underlying degradation mechanisms as low-temperature sputtered, industrially-compatible NiO_x is altered, but not omitted or substituted with other HTLs. Therefore, this study investigates four HTLs – NiO_x, copper-doped NiO_x (NiO_x:Cu), and their passivated forms with MeO-2PACz SAM (NiO_x + SAM and NiO_x:Cu + SAM) – and their impact on the cells' stability by combining experimental and modeling techniques.

On the experimental side, we have performed device characterization (*JV* scans), aging/stability tracking (continuous MPP tracking over two weeks) and HTL–perovskite interface characterization *via* transient surface photovoltage, tr-SPV, (transient) photoluminesence, (Tr)PL, and ultraviolet photoemission spectroscopy (UPS) measurements.

On the modeling side, we have simulated the *JV* curves of fresh and two-week-aged solar cells with the varying HTLs *via* steady-state drift-diffusion simulations, which used many of the experimentally-obtained values as input parameters. The steady-state drift-diffusion simulations rely on the publicly-available SIMsalabim simulation software[62,63] and enable a variety of important parameters that contain information on interfaces in the device, band diagrams, density of traps at the interfaces, and all relevant recombination mechanisms (direct, bulk trap-assisted, and interface trap-assisted recombination) to be extracted. Additionally, unlike SCAPS[64,65] and other 1D drift-diffusion simulation software, SIMsalabim accounts for mobile ionic species, which are of paramount importance when evaluating the stability, hysteresis, and non-radiative recombination processes in perovskite-based solar cells.[66] Other drift-diffusion simulation software tools that also consider mobile ions are DriftFusion[67] and IonMonger.[15,16,68,69] IonMonger, in particular, works in a similar manner to SIMsalabim, as both simulation tools use the input parameters to numerically solve the Poisson, the continuity, and the drift-diffusion equations.

We also disclose that the V_{oc} statistics, the tr-SPV, the TrPL, and the UPS measurements have already been published in ref. 18. As will be discussed in the Methods section, this data is revisited in this publication as several of these measurements are used as input parameters for the simulations or to validate the accuracy of the simulated results. Despite the fact that the HTL configurations are the same in both works, their fundamental questions are greatly different. This paper primarily wants to understand the degradation mechanisms in the cells *via* the simulations, while the paper which contains the here-used input parameters[18] was primarily focusing on developing highly-efficient CIGS–perovskite tandem solar cells *via* HTL optimization. The stability of the cells was not investigated, neither in the single-junction nor the tandem configuration, but the fact that the same HTLs are used gives us a unique opportunity to obtain and fix many of the input parameters *via* experimental measurements.

By combining the measured and simulated results, we investigate three important aspects of these devices: (1) the impact of the energy alignment and interfaces on the charge-carrier extraction and trapping; (2) the influence of the recombination mechanisms on the stability of the solar cells; and (3) the role of (mobile) ions on the hysteresis factor detected in the *JV* scans. Out of these three sections, only the first one relies on the previously-published experimental data, serving to benchmark the model against the experimental results. Once validated, the model is applied in the subsequent two sections, which present results solely obtained from the simulations. Thus, by simulating the *JV* curves of the fresh and the aged single-junction perovskite solar cells, by altering only the HTL, and by investigating how the above-mentioned aspects change as the devices age, one can, to the best of the model's ability, better understand what the stability-limiting factors in the cells are.

Finally, we point out that fitting of *JV* curves is not *per se* a novel technique, but most studies focus exclusively on the fits of as-deposited (fresh) cells, while the improvement in the stability is only shown with MPP tracking. However, when doing so, a plethora of untapped information available in the degraded *JV* curves is left behind. With this study, we want to point out that fitting both curves can push our knowledge on the degradation pathways even further and provide a fundamental understanding of the physical processes that govern the degradation of single-junction perovskite solar cells. This dual experimental–modeling approach, particularly the simulation of aged *JV* curves to extract degradation pathways, is rare in the field and provides an untapped method for understanding long-term performance losses. As such, this method can further be applied to novel cell configurations with other HTLs and possibly even two-terminal tandem solar cells, which would use an identical perovskite device as the top device.

2. Methods

The *JV* and aging measurements as well as the steady-state drift-diffusion simulations of the single-junction perovskite solar cells are performed on single-junction perovskite solar cells with four varying hole-transporting layers (HTLs): 20-nm-thick nickel oxide (NiO_x) or 2% copper-doped nickel oxide (NiO_x:Cu) with or without MeO-2PACz ([2-(3,6-dimethoxy-9*H*-carbazol-9-yl)ethyl]phosphonic acid) self-assembled monolayer (SAM) surface passivation (NiO_x + SAM and NiO_x:Cu + SAM). The transient surface photovoltage (tr-SPV), transient photoluminescence (TrPL) measurements, and ultraviolet photoemission spectroscopy (UPS) were performed on an ITO + HTL + perovskite stack to diminish the impact of the ETL.

2.1. Hole-transporting layer and solar-cell preparation

The substrate for all cells is patterned ITO, enabling us to get 6 solar cells with an active area of 0.16 cm^2 (referred to as pixels) per one ITO substrate. The substrate for the partial stacks used for the tr-SPV, TrPL, and UPS measurements is non-patterned ITO. Both types of ITO are ultrasonically cleaned for 15 minutes in soap, DI water, acetone, and isopropanol, after which the substrates are moved to an UV–ozone cleaner for an additional 15 minutes.

20-nm-thick nickel oxide (NiO_x) is RF sputtered at a low-temperature (no additional heating during sputtering) and is not subjected to any annealing treatment post sputtering. Two sputtering targets were used: NiO_x (99.9% purity, manufacturer Nova Fabrica) and NiO_x:Cu (2%Cu doping, manufacturer Nova Fabrica). The sputtering was performed in a pure Ar (99.999%) atmosphere. The power, the pressure, and the target-to-sample distance were kept constant for all samples at 60 W, $(4.7 \pm 0.1) \times 10^3$ mbar, and 5 cm, respectively. Once the sputtering was completed, the samples were transferred to and sealed in a N_2-filled glovebox. The samples with NiO_x(:Cu) as a stand-alone HTL were then opened in another N_2-filled glovebox for the perovskite deposition, while the samples onto which SAM was deposited were subjected to 15-minute ozone cleaning treatment.

A 1mM solution of MeO-2PACz ([2-(3,6-dimethoxy-9*H*-carbazol-9-yl)ethyl]phosphonic acid) self-assembled monolayer is prepared by mixing the SAM powder (TCI) in anhydrous ethanol (VWR Chemicals). 100 μl of this solution are then spin-coated on top of the NiO_x(:Cu) at a speed of 4000 rps for 45 seconds, followed by annealing at 100 °C for 10 minutes.

All of the samples undergo perovskite deposition. A triple-cation perovskite $(Cs_{0.05}(MA_{0.17}FA_{0.83})_{0.95}Pb(I_{0.83}Br_{0.17})_3$-(CsMAFA), $E_g = 1.63$ eV)[70] is used consistently. PbI_2 and $PbBr_2$ salts (99.99% purity, TCI) are mixed with a 4 : 1 DMF : DMSO mixture (DMF: *N*,*N*-dimethylformamide, DMSO: dimethylsulfoxide, Sigma-Aldrich) and shaken overnight at 60 °C. The next day, a FAI salt (formamidinium iodide, 99.99% purity, Dyenamo) is mixed with the PbI_2 solution to produce a $FAPbI_3$ (formamidinium lead iodide) solution. The $PbBr_2$ is mixed with a MABr salt (methylammonium bromide, 99.99% purity, Dyenamo) to yield a $MAPbBr_3$ (methylammonium lead bromide) solution. A third solution of CsI is prepared by dissolving CsI salt (cesium iodide, 99.999% Cs) in DMSO. No shaking or heating is needed. The triple-cation perovskite solution is then produced by combining all three solutions – $FAPbI_3$, $MAPbBr_3$, and CsI – into one solution. The $FAPbI_3$ and $MAPbBr_3$ are mixed in an 83 : 17 ratio and represent 95% of the total solution, while the CsI makes the remaining 5%.

Then, 100 μl of the perovskite solution are spin-coated on top of the HTL at a speed of 4000 rpm for 40 seconds. The anti-solvent is ethyl acetate (anhydrous, 99.8% purity, Sigma-Aldrich) and 500 μl of it are applied drop-wise on the 25th second of spin-coating. The cells are then annealed at a temperature of 100 °C for 60 minutes. Subsequently, the cells are transferred to another N_2-filled glovebox for the deposition of the ETL, which, the same as the perovskite, remains unchanged throughout the whole study. First, 23-nm-thick C_{60} is evaporated under vacuum and then 20-nm-thick tin oxide (SnO_2) is applied *via* ALD. The metal grid is a Cu (copper) one, evaporated under vacuum.

2.2. *JV* measurements and MPP tracking

The *JV* measurements were performed in a N_2 glove box using an Oriel class ABB sun simulator under simulated illumination with an AM 1.5 G spectrum. No light-soaking or biasing is used. Each cell is measured in both a forward-bias ($V_{start} < V_{end}$) and reverse-bias ($V_{start} > V_{end}$) scan direction. The scanning speed was 0.5 V s^{-1}, but for the discussion of the hysteresis factor

(HF), measurements at scan speeds of 0.1, 0.2, 0.25, 0.5, and 1 V s^{-1} were also performed.

The cells were aged in a high-throughput aging system explained in detail in ref. 71. The cells were aged for two weeks under continuous illumination under a simulated AM1.5 G spectrum using a metal-halide lamp and at a temperature of 25 °C. No pre-aging or pre-conditioning procedure was employed. The system has air-tight, nitrogen-filled sample boxes that fit eight substrates, each with six pixel-like solar-cells (area = 0.16 cm^2). Continuous MPP tracking is achieved *via* custom-made MPPT electronics[71] and a *JV* curve is recorded every 24 hours. Since each aging box fits eight substrates, there were two substrates per HTL. As each substrate has 6 pixel-like solar cells, the aging curve per HTL is an averaged curve from 12 pixel-like solar-cells.

In addition to the 2 substrates (12 pixels) that were aged, we also report statistics of *JV* parameters from 44 pixel-like solar cells. These *JV* measurements were conducted in a N_2 environment with an Oriel class ABB sun simulator under simulated illumination with an AM 1.5 G spectrum with no previous light soaking or biasing. When calculating the quasi-Fermi level splitting (QFLS) to V_{oc} offset, we consider the QFLS measured *via* absolute PL measurements and the median V_{oc} value of the 44 measured V_{oc} values.

2.3. Drift-diffusion simulations

The 1D steady-state drift-diffusion simulations are performed with open-source Pascal-based SIMsalabim software[62] available on GitHub.[63] The simulations account for both the diffusion and the drift currents that move the charge carriers in the solar cells, the impact of ions' screening, despite being performed under steady-state conditions, and the two dominant recombination mechanisms in perovskite solar cells: radiative and trap-assisted Shockley–Read–Hall recombination, where the latter also distinguished between bulk and interfacial trapping.

SIMsalabim is based on the continuity, charge-transport, and Poisson equations to simulate varying *JV* curves. The continuity equation accommodates the fact that ions – either vacancies or interstitials – might also be mobile in the perovskite solar cells by adopting the following form:

$$\frac{\partial X_{\text{ion}}}{\partial t} = \frac{1}{e}\frac{\partial}{\partial x}\left(-eX_{\text{ion}}\mu_{\text{ion}}\frac{\partial V}{\partial x} \pm eD_{\text{ion}}\frac{\partial X_{\text{ion}}}{\partial x}\right), \tag{1}$$

where X refers to the density of ions, "ion" stands either for anion (X_a) or cation (X_c); x is the spatial coordinate, namely thickness of the cell, $x = 0$ is set for the cathode, $x = L$ for the anode; t = time, describes how the ion distribution evolves over time; D = carrier diffusion coefficient and μ = ion mobility. The simulations in this paper were limited to ionic movement within the perovskite layer only, in agreement with various reports in the literature.[13,72–74]

The charge-transport equation defines the electron and hole currents due to diffusion or drifting as

$$j_i = -ei\mu_i\frac{\partial V}{\partial x} \pm eD_i\frac{\partial i}{\partial x}, \tag{2}$$

where i denotes the carrier density n or p (or as a subscript indicates the corresponding carrier type) and $D_i = \mu_i\frac{k_BT}{e}$ is the carrier diffusion coefficient.[66]

Finally, the Poisson equation $\frac{\partial}{\partial x}\left(\epsilon\frac{\partial V}{\partial x}\right) = -e(p - n - C_i)$, where C_i is any type of charge in the system, is adjusted to accommodate all potential charges in the investigated system, such as doping (especially in the transport layers, where a distinction between ionized p-type (N_A^-) and n-type (N_D^+) doping is made), density of ions (X_a and X_c), and charge traps (Σ_T^+ for holes and Σ_T^- for electrons). Therefore, SIMsalabim uses the following form of the Poisson equation:

$$\frac{\partial}{\partial x}\left(\epsilon\frac{\partial V}{\partial x}\right) = -e\left(p - n + N_D{}^+ - N_A{}^- + X_c - X_a + \Sigma_T{}^+ - \Sigma_T{}^-\right). \tag{3}$$

N_D: ionized donor concentration, N_A: ionized acceptor concentration.

These three equations are solved numerically by using well-defined boundary conditions. First, for the carrier densities $n(0)$ and $p(0)$,

$$n(0) = N_C\exp\left(-\frac{\phi_n}{V_T}\right), \tag{4}$$

$$p(0) = N_V\exp\left(-\frac{E_g - \phi_n}{V_T}\right). \tag{5}$$

Here N_C and N_V are the effective densities of states of the conduction band and the valence band respectively, and E_g is the bandgap of the semiconductor. Second, for the carrier densities $n(L)$ and $p(L)$,

$$n(L) = N_C\exp\left(-\frac{E_g - \phi_p}{V_T}\right), \tag{6}$$

$$p(L) = N_V\exp\left(-\frac{\phi_p}{V_T}\right), \tag{7}$$

where ϕ_i is the electron ($i = n$) or hole ($i = p$) injection barrier at the cathode/anode, L is the total simulated thickness (ETL + perovskite thickness + HTL) and $V_T = \frac{k_BT}{e}$ is the thermal voltage. Third, for the potential at the contacts,

$$e(V(L) - V(0) + V_{\text{applied}}) = W_c - W_a, \tag{8}$$

where W_c and W_a are the cathode's and anode's work functions, respectively. The cathode is set at $x = 0$ and the anode at $x = L$.[66]

For the recombination types, the following equations are used:

$$R_{\text{SRH}} = \frac{C_nC_p\Sigma_T}{C_n(n + n_1) + C_p(p + p_1)}\left(np - n_i{}^2\right), \tag{9}$$

$$n_1 = N_c\exp\left(-\frac{E_C - E_{\text{trap}}}{k_BT}\right)\text{and } p_1 = N_v\exp\left(-\frac{E_{\text{trap}} - E_V}{k_BT}\right) \tag{10}$$

$$R_{\mathrm{dir}} = k_2(np - n_i^2). \tag{11}$$

where E_c is the conduction band edge energy, E_{trap} is the trap energy level and k_2 is the direct (radiative) recombination coefficient.

Thus, SIMsalabim allows for a decomposition per recombination type (trap-assisted Shockley-Read-Hall recombination and direct). At V_{oc}, the steady-state requirement is that the spatially integrated photogeneration equals the spatially integrated recombination, *i.e.*

$$q\int_0^L G(x)\mathrm{d}x = q\int_0^L R(x, V_{\mathrm{oc}}\mathrm{d}x). \tag{12}$$

Moreover, under V_{oc} conditions, it is even better to verify that $J_{\mathrm{Recombination}}$ (to be obtained by summing up all three J values shown in Fig. 7 at V_{oc} – namely, direct, bulk SRH, and interface SRH recombination current densities) equals $J_{\mathrm{gen}} = q\int_0^L G(x)\mathrm{d}x = qGL$ (shown in Fig. 1) – confirming that generation and recombination are fully balanced under open-circuit conditions and that the simulations are consistent.

In this work, SIMsalabim is used to fit experimentally measured *JV* curves at the start of the aging procedure (fresh solar cells) and at the end of the aging procedure (aged solar cell). The simulations are performed by using a set of common physical parameters, such as VBM, CBM, charge mobilities, and generation rates, as input parameters[66] to numerically solve eqn (1)–(3), which then generate *JV* curves and yield information on the recombination dynamics in the devices. The order of the fitting parameters is pre-set in an input-parameter file, but it is irrelevant in which order the parameters are updated in this file. However, fitting the experimental *JV* curve comes with its own challenges, primarily because not all of the input parameters can be obtained experimentally for each investigated solar cell.[66]

The input parameters can be broadly grouped into seven categories: general, mobilities, contacts, transport layers (both HTL and ETL), ions, generation and recombination, and trapping.

To diminish the number of input parameters taken from the literature, the following parameters were experimentally measured or controlled: the thicknesses of the ETL, HTL, and the perovskite; the VBM and CBM of the perovskite; the doping of the HTL; the generation rate of electron–hole pairs; the bulk trap density; and the interface trap density at the HTL–perovskite interface. The remaining parameters were taken from the literature.

The only parameters that were altered as the cells aged were the mobilities (to accommodate for the change in the FF in the aged cells), the generation of electron–hole pairs (to accommodate for the change in the J_{sc} in the aged cells), and the bulk trap density (to accommodate for the change in the V_{oc} in the aged cells). A complete list of the values of all input parameters for all HTLs (before and after aging) is presented in the SI, while here we elaborate in a bit more depth on how the experimentally measured inputs were obtained.

The simulation model considers the valence band maximum (VBM) and the conduction band minimum (CBM) positions of the electron-transport layer (ETL), the absorber (perovskite), and the hole-transporting layer (HTL). The electronically degenerate contacts are defined solely by their respective work function (WF).

The input parameters for the VBM of the perovskite are derived from UPS measurements conducted on the ITO/HTL/perovskite stack (Fig. 3b and SI). Since each hole transport layer (HTL) alters the WF and VBM of the perovskite, the resulting VBM and CBM values vary depending on the specific HTL used. In the simulations, the VBM is referenced to the vacuum level. Therefore, the VBM input is calculated as the sum of the measured WF and the VBM (relative to the Fermi level). The CBM is then obtained by subtracting the perovskite bandgap (1.63 eV) from this VBM value. For example, UPS measurements for NiO_x yield a WF of 4.6 eV and a VBM located 1.5 eV below the Fermi level, resulting in an input VBM of 6.1 eV (4.6 + 1.5) and a CBM of 4.47 eV (6.1 − 1.63). This procedure is applied consistently across all HTLs to determine the input parameters for both the perovskite and the HTLs.

The average generation of electron–hole pairs G_{ehp} was calculated from the short-circuit current density J_{sc} in the *JV* curves of the solar cells by using the relation $J_{\mathrm{sc}} = qG_{\mathrm{ehp}}L$, where q is the elementary charge and L is the thickness.

The total simulated thickness L is set to 643 nm: 23 nm of C_{60}, 600 nm of perovskite, and 20 nm of NiO_x(:Cu). Since SAM is a monolayer, its thickness was neglected.

The doping and the mobility in the HTL were obtained from Hall measurements for NiO_x(:Cu) and it was assumed that passivating the NiO_x(:Cu) surface with SAM does not change the doping in the bulk of the NiO_x(:Cu).

The density of bulk traps in the perovskite (also referred to as the bulk trap density (BTD) in the perovskite) is calculated from the effective PL lifetimes presented in Fig. 4 and measured *via* time-resolved photoluminesence measurements. The BTD was then calculated from the PL effective lifetimes (τ_{eff}) by using $\mathrm{BTP} = \dfrac{1}{\tau_{\mathrm{eff}} \times C_\mathrm{p}}$, where C_p is the capture coefficient for holes. Note that the trap coefficients for electrons and holes (C_n and C_p) are taken from the literature and are kept equal and fixed across all simulations.

In terms of the ETL, it should be noted that if there is an input parameter for the HTL, there is an accompanying input parameter for the ETL as well. The difference is, as the HTLs are varied and experimentally quantified, the input parameters can vary. However, as the ETL is the same in all of the devices (C_{60}) and beyond the scope of this investigation, many of the input parameters referring to it are obtained from the literature and kept constant for all cell configurations and regardless of whether the cells are fresh or aged. The only exception is its CBM and VBM, which inevitably change when the perovskite CBM and VBM change as the HTL is changed.

Finally, it is important to elaborate on the notation and the output parameters of the simulations.

In addition to a simulated *JV* curve, which can be compared to the experimentally-measured one, the simulations yield also the following results: a band diagram for each cell configuration with a varying HTL and the rates of recombination, decomposed per type. Additionally, we also discuss the impact of the density of interface and bulk traps, as well as the density of ions.

With respect to the notation, many of the explanations contain the subscripts "-n" and "-p". These refer to the ETL and HTL contact, respectively. For instance, $R_{\text{Int-SRH-n}}$ is the interface recombination at the ETL interface and $R_{\text{Int-SRH-p}}$ is the interface recombination at the HTL interface, but they do not refer to the type of traps. However, since the ETL is always the same (C_{60} + SnO_2) and the HTL is varied, we attribute any changes in electron trapping at the ETL–perovskite or hole trapping at the HTL–perovskite interface to the HTL, or rather to the overall charge-carrier dynamics in the cell due to the respective HTL.

2.3.1. The impact of the ions' screening. Ion migration and its relation to the detected hysteresis in perovskite solar cells have lately been investigated *via* the time-resolved coupled ion drift-diffusion simulation model.[13,14] The simulations are also often performed for measurements at varying scan speeds, due to the reasons mentioned above. In principle, the time-resolved simulations are based on the same model used for the here-presented steady-state drift-diffusion simulations and both include the effect of ionic species. The difference is that the steady-state simulations give an output current for the ionic movement at a given voltage across the device length, while the time-resolved simulations can perform a full transient movement of ions. Since ion-induced hysteresis is very much dependent on the time between two applied potentials (namely, the scan speed), the transient simulations are the better choice for the hysteresis investigation.

Nevertheless, the steady-state simulations can also give a first look into the ionic concentration and if needed, movement across the simulated device length. An insightful parameter to do this is the hysteresis factor (HF), calculated from the *JV* curves as:[13]

$$\mathrm{HF} = \frac{A\left(\left|J_{\text{rev.}} - J_{\text{forw.}}\right|\right)}{A\left(J_{\text{rev.}}\right)}, \tag{13}$$

where $A(J)$ is the area under the *JV* curve measured either in the reverse- or forward-bias direction and is defined as:

$$A(J) = \int_{V=0}^{V=V_{\text{oc}}} J(V)\mathrm{d}V. \tag{14}$$

The HF was evaluated for a scan speed of 0.5 V s^{-1}, at a voltage step of 0.02 V, and an integration time of 40 ms as the default measurement settings. The ion concentrations were fine-tuned until the simulated *JV* curves shown with dashed lines in Fig. 1 yielded a FF and R_{sh} that matched those of the measured *JV* curves shown with solid lines.

These steady-state drift-diffusion simulations allow setting whether negative, positive, or both types of ion move into the perovskite. The results presented here were obtained by allowing both ion species to be mobile. Allowing either positive or negative ions to move was also tested, but such specifications caused a mismatch between the simulated and the measured R_{sh}. A more in-depth discussion on why both ionic species can move is presented in the Results section.

2.4. Charge-carrier dynamics at the HTL–perovskite interface

Transient surface photovoltage (tr-SPV) measurements, transient photoluminescence (TrPL) measurements, and ultraviolet photoemission spectroscopy (UPS) were performed on an ITO + HTL + perovskite stack to diminish the impact of the ETL. The HTL and the perovskite were deposited in the same manner as in the solar cells. These measurements were used for the above-mentioned input parameters in the simulations.

The time-resolved photoluminescence (TrPL) measurements were conducted using a 660 nm pulsed laser diode, with an excitation spot diameter of approximately 110 μm and an average intensity of 100 nW. The emitted photoluminescence was filtered by a 700 nm long-pass filter, and the time-correlated single-photon counting technique allowed signal detection for approximately 4 μs. The injected carrier concentration, averaged over the perovskite absorber thickness (500 nm), was around 10^{15} cm^{-3} per laser pulse at a TrPL repetition rate of 125 kHz, corresponding to near 1-sun conditions.

For the time-resolved surface photovoltage (tr-SPV) measurements, a pulsed 515 nm excitation laser with a 5 mm spot size, 8 μs signal duration, and 125 kHz excitation-pulse repetition rate was used. The photo-excitation was performed from the perovskite side. Since the excitation pulse repetition rate was the same for both the TrPL and the tr-SPV measurements, they can be synchronized. Thus, the tr-SPV measurements are also averaged over the perovskite thickness of 500 nm and the injected carrier concentration was 10^{15} cm^{-3} The laser fluence was controlled using neutral density filters and monitored with a power meter. The SPV signal was measured in a parallel-plate capacitor configuration, consisting of a quartz cylinder partially coated with an SnO_2:F electrode and a mica sheet as an insulator.

The UPS measurements were conducted in a vacuum atmosphere at a pressure of around 10^{-7} mbar, at an acceleration voltage of 15 V, and a lamp current of approximately 30 mA. For the detailed measurements of the secondary electron edge (SEE) and the valence band (VB), a UV HeI source (21.1 eV excitation energy) with a pass energy of 2.5 eV and with a step of 0.01 eV is used. The SEE has a much better signal-to-noise ratio than the VBM, so usually no more than 10 repeat scans were performed. For the VBM, usually between 50 to 70 repeat measurements were performed in order to obtain a less noisy leading VB edge. The UPS measurements, as well as the procedure as to how the work function (WF) and the VBM are calculated, are all presented in the SI.

3. Results

We start by choosing representative, experimentally-obtained *JV* curves of both fresh and aged solar cells with each HTL and then simulate them with SIMsalabim (Fig. 1). These fits display an R^2 value of around 0.99, indicating an excellent agreement with the measured *JV* curves. The other *JV* curves can be found in the SI.

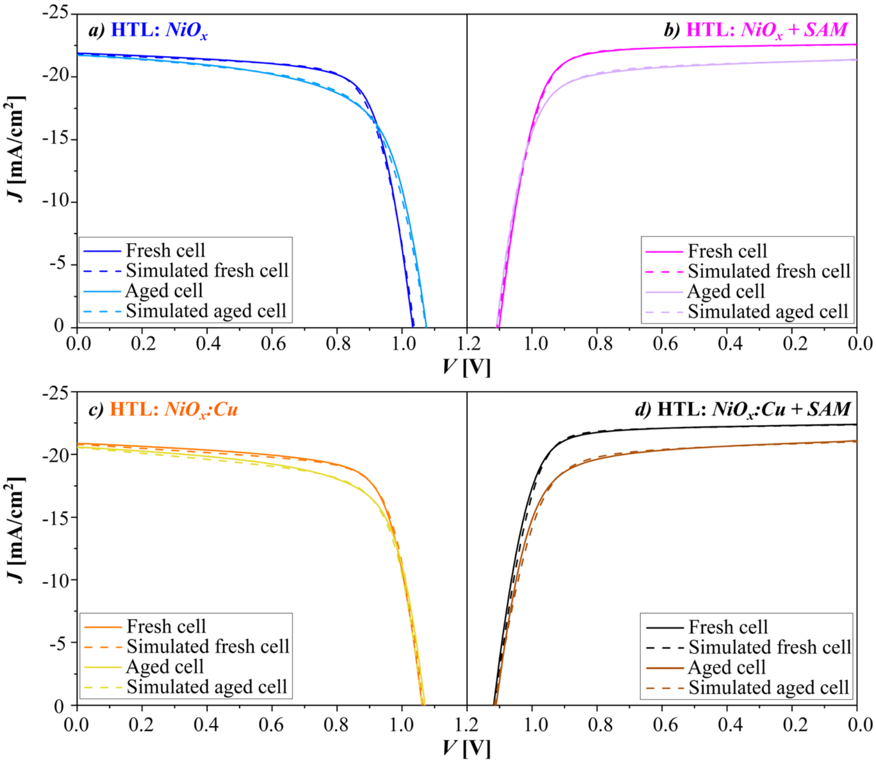

Fig. 1 Experimentally-measured (solid lines) and simulated (dashed lines) *JV* curves of single-junction perovskite solar cells (a) NiO$_x$ (blue shades), (b) NiO$_x$ + SAM (magenta shades), (c) NiO$_x$:Cu (orange shades), and (d) NiO$_x$:Cu + SAM (black and brown color) before and after two-week MPP tracking under constant AM1.5 G illumination in N$_2$ environment and at 25 °C.

The simulations of the fresh and the aged cells presented in Fig. 1 enable us to structure our discussion around two subtopics. First, for the fresh solar cells, we discuss their simulated band diagrams by considering the measured and the simulated QFLS–V_{oc} offset on the one hand and the charge-carrier dynamics (trapping, extraction and recombination of carriers) at the HTL–perovskite interface or in the perovskite bulk on the other hand. Second, the long-term stability of the solar cells is discussed by correlating the aging experiments to the simulated results for both the fresh and the aged cells, enabling us to pin-point the cells' dominant recombination mechanisms and their progression over time. Note that the first discussion merges experimental and simulated results to not only connect the two, but also to test the validity of the simulations. Once we show a good agreement between the experiential and the simulated data, the latter can be used exclusively to discuss the main degradation pathways in the cells.

3.1. Impact of energy alignment and interfaces on charge-carrier trapping and QFLS–V_{oc} offsets

The simulated band diagrams under open-circuit (V_{oc}) conditions are shown in Fig. 2.

Before discussing the results in more detail, it should be mentioned that both the simulated and the measured QFLS of the bare perovskite absorber (without an ETL or HTL) is smaller than the theoretical maximum V_{oc} ($=$ QFLS$_{rad.}$) obtained *via* a detailed-balance (Shockley–Queisser) calculation in the radiative limit, due to non-negligible non-radiative (SRH) losses.[75] The simulated QFLS in the perovskite bulk in Fig. 2 is around (1.24 ± 0.01) eV, which agrees well with the measured 1.23 eV QFLS in triple-cation perovskites in other works.[76] This QFLS is then suppressed by the incorporation of the HTLs, resulting in a measured QFLS on the ITO + HTL + perovskite stack in the range of 1.14 to 1.18 eV, as presented in Fig. 3. The QFLS–V_{oc} offset is then calculated by subtracting the median value of the V_{oc} from the QFLS.

Ideally, to have as small as possible QFLS–V_{oc} offsets, both charge-selective layers (ETL and HTL) need to be as selective as possible, namely with a small or negligible band offset to the perovskite absorber.[76] Additionally, the trapping at the CSLs–perovskite interfaces should also be diminished in order to suppress the interfacial recombination.[77] For the HTL and ETL, the offsets of interest are the valence band maximum (VBM) and the conduction band minimum (CBM), respectively. The metal contacts do not induce significant losses compared to the interfacial losses at the ETL– and HTL–perovskite interfaces.[78]

Taking this into consideration, we detect that NiO$_x$ has the most unfavorable band alignment among all four HTLs. A non-negligible 0.36 eV energetic offset at the HTL–perovskite interface results in a strong band misalignment and spike formation at the valence band maximum, pinning the Fermi level at the interface (Fig. 2a). The C$_{60}$–perovskite interface with its 0.09 eV spike is also unfavorable. Nevertheless, the NiO$_x$–perovskite interface is the limiting interface in this cell configuration,

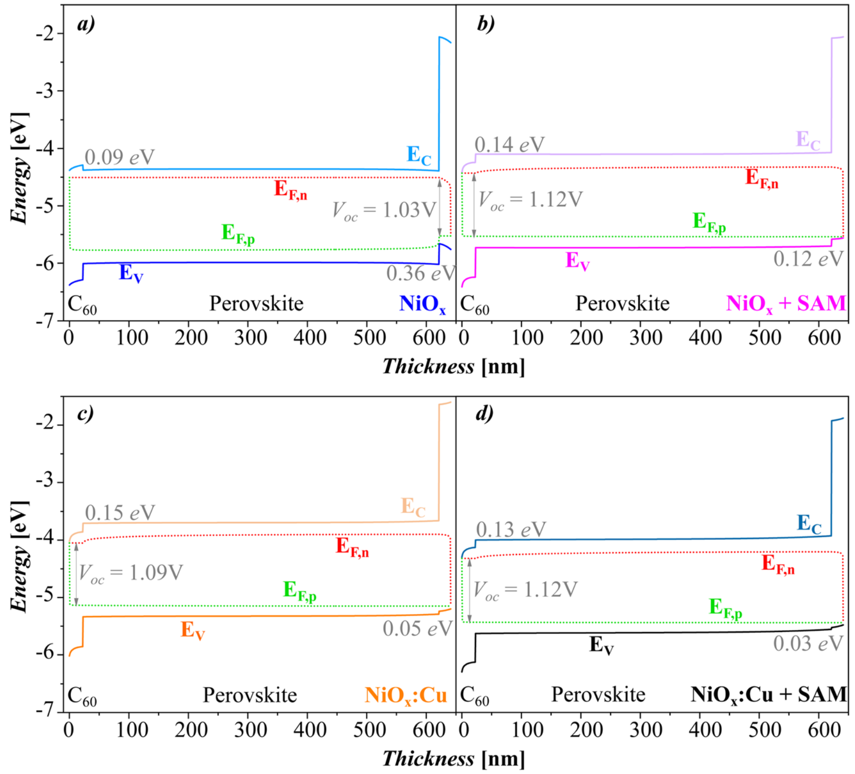

Fig. 2 Simulated band diagrams at V_{oc} of single-junction perovskite solar cells under illumination, with (a) NiO_x (blue shades), (b) NiO_x + SAM (magenta shades), (c) NiO_x:Cu (orange shades), and (d) NiO_x:Cu + SAM (black and brown color). The quasi-Fermi levels are marked in red ($E_{F,n}$) and in green ($E_{F,p}$). The exact values of the band offsets at the HTL–perovskite and ETL–perovskite interfaces are written in grey text. A more prominent energetic barrier is seen at the ETL–perovskite interface for all HTLs, except for NiO_x (band offset (ETL–pero) > band offset (HTL–pero)).

since it induces a more severe band misalignment at the VBM than the band misalignment that the C_{60}–perovskite interface induces at the CBM.[76] Therefore, in the NiO_x-based perovskite solar cells, the hole transporting layer (NiO_x) and not the electron-transporting layer (C_{60}) causes the dominant V_{oc} loss, which always occurs at the inferior interface.[76,78]

The remaining three HTL configurations (NiO_x:Cu, NiO_x + SAM, and NiO_x:Cu + SAM, Fig. 2b–d) display more favorable band alignment compared to NiO_x. Passivating the NiO_x surface with a SAM significantly decreases the 0.36 eV offset at the HTL–perovskite interface down to 0.12 eV and improves the device's V_{oc}, while the band offset for NiO_x:Cu (+SAM) at the HTL–perovskite interface is close to zero. The V_{oc} losses for these three devices are predominantly occurring at the C_{60}–perovskite interface.

The significant misalignment at the NiO_x–perovskite interface is most likely also the reason why NiO_x displays the most prominent QFLS–V_{oc} offset among all four-investigated HTLs.[76,78] This can clearly be seen from the linear correlation in Fig. 3c between the total measured QFLS–V_{oc} offset (extracted from Fig. 3a) and the total simulated misalignment in the devices (the sum of the energetic offsets at both interfaces, as simulated in Fig. 2).

This result can also be corroborated when looking at the UPS measurements performed on an ITO + HTL + perovskite stack (Fig. 3b) that were used as input parameters in the simulations for the VBM and the CBM of the perovskite. The UPS measurements indicate that the underlying HTL can induce electronic changes in the bulk of the perovskite by shifting its Fermi level, conduction band minima and valence band maxima positions, as discussed in more detail in ref. 18. Specifically for NiO_x, we see that this HTL shifts the Fermi level in the perovskite so prominently that the perovskite can no longer be considered an intrinsic material. The offset between the perovskite's Fermi level and the CBM is only 0.13 eV, making the perovskite absorber an n-type material and leading to the most prominent band misalignment among all four HTLs.

Other than the QFLS–V_{oc} offset, it is also instructive to look at the absolute value of the measured QFLS, independent of its relation to the device's V_{oc}. Fig. 3a indicates that although NiO_x:Cu (+SAM) has a low QFLS–V_{oc} offset, its QFLS is actually lower than the QFLS of NiO_x (+SAM). To better understand this behavior, we take a look at four aspects: (1) the trapping of holes at the HTL–perovskite interface; (2) the trapping of electrons at the HTL–perovskite interface; (3) the rate of hole extraction by each HTL; and (4) the recombination rates in the perovskite with each HTL. A similar discussion can be found in ref. 77, where the authors detected a trend between a loss in the V_{oc} and band misalignment, but further investigated the role of

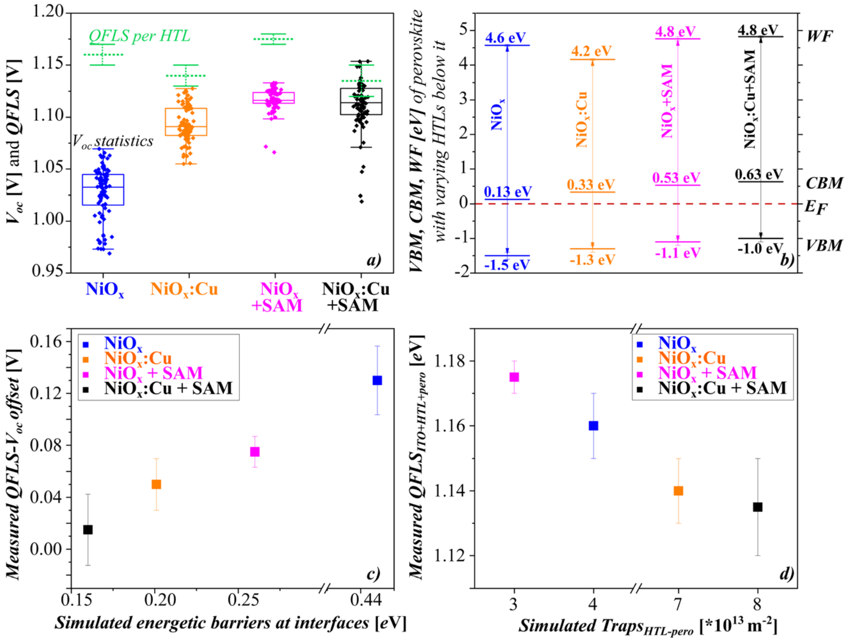

Fig. 3 (a) V_{oc} statistics and the QLFS (in light-green color) per HTL; (b) UPS measurements of ITO + HTL + perovskite samples with all four HTLs; (c) measured QFLS–V_{oc} offset as a function of the total simulated energetic barrier (at both ETL– and HTL–perovskite interfaces) in the single-junction perovskite solar cells under illumination; and (d) measured absolute QFLS as a function of the total simulated trap density at the HTL–perovskite interface. The QFLS was measured *via* absolute PL measurements. Sub-figures (a) and (b) have already been published in ref. 18.

trapping of minority carriers at the interfaces (point (2) in our discussion).

First, in Fig. 3d we correlate the number of (simulated) traps for holes at the HTL–perovskite interface (Simulated $\text{Traps}_{\text{HTL-pero}}$) with the absolute QFLS value (Measured $\text{QFLS}_{\text{ITO+HTL+pero}}$). We see that a lower number of interfacial traps for holes at the HTL–perovskite interface leads to a higher QFLS in the bulk of the perovskite with a given HTL. In this aspect, NiO_x (+SAM) is a superior HTL compared to NiO_x:Cu (+SAM) since it traps less holes at the NiO_x (+SAM)–perovskite interface.

Next, in Fig. 4 we present the transient surface photovoltage (tr-SPV) and time-resolved photoluminesence (TrPL) measurements on ITO + HTL + perovskite stacks to better investigate the trapping of the electrons, the rate of hole extraction by each HTL, and the recombination rates in the perovskite with each HTL. We then correlate these measurements with the simulated rates of bulk SRH ($R_{\text{bulk-SRH}}$) and interface SRH for electron capture ($R_{\text{Int-SRH-n}}$) recombination extracted at the V_{oc} point for the solar cells.

When analyzing tr-SPV measurements for the charge-carrier dynamics at the interface, one should consider two aspects.[79] First, positive tr-SPV signals indicate electron trapping at the HTL–perovskite interface. Second, the quicker the tr-SPV minimum is reached, the faster the extraction of the holes. As NiO_x is the only HTL with positive tr-SPV signals, and as its minimum is reached the latest among all four HTLs, we conclude that NiO_x traps electrons and does not extract holes efficiently at the HTL–perovskite interface.

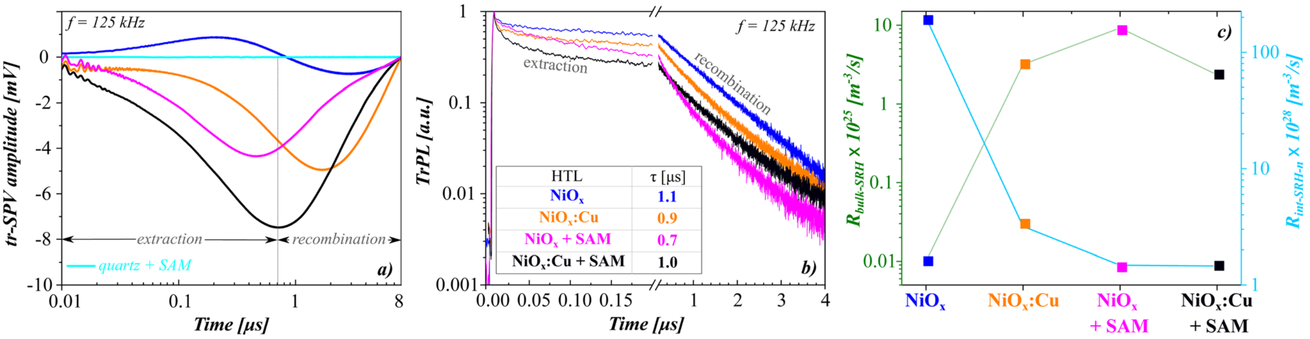

Fig. 4 (a) tr-SPV measurements for NiO_x (blue), NiO_x:Cu (orange), NiO_x + SAM (magenta) and NiO_x:Cu + SAM (black) and a reference (mint; quartz + SAM); (b) TrPL measurements; (c) simulated rates of bulk SRH ($R_{\text{bulk-SRH}}$) and interface SRH recombination at the ETL–perovskite interface ($R_{\text{Int-SRH-n}}$) extracted at the V_{oc} point for the solar cells. The tr-SPV and the TrPL measurements were conducted on the same ITO + HTL + perovskite stacks at an equivalent frequency of 125 kHz to allow for a direct comparison of the results. Sub-figures (a) and (b) have already been published in ref. 18.

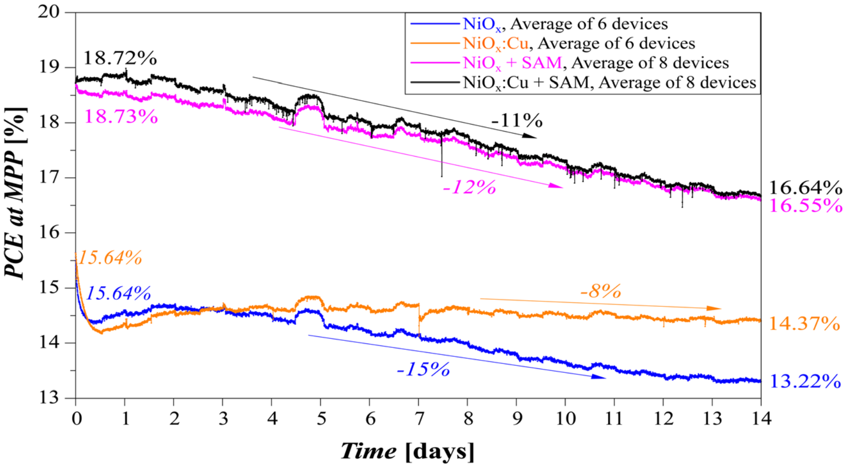

Fig. 5 Two-weeks of continuous MPP tracking of p-i-n single-junction perovskite solar cells with NiO$_x$(:Cu) (+SAM) HTLs and C_{60}–SnO_2 as the ETL stack at a temperature of 25 °C, in a N_2 atmosphere, and without encapsulation. The given loss in the MPP is relative, namely NiO$_x$:Cu loses 8% of its initial PCE at the MPP, while NiO$_x$ loses 15%.

The argument of electron trapping is also strengthened by the steady-state drift-diffusion simulations, which indicate that NiO$_x$ has ~66 and ~130 times stronger recombination *via* interface traps for electrons ($R_{\text{Int-SRH-n}}$) than NiO$_x$:Cu and NiO$_x$(:Cu) + SAM (for more details, refer to Fig. 6b in Subsection 3.2). Finally, the Tr-PL measurements also confirm that NiO$_x$ has the poorest hole-extraction capability among the four-investigated HTLs, as the decay of the Tr-PL signal in the extraction regime is the weakest.

Interestingly, however, in the recombination regime, and thus in the effective lifetime, the TrPL measurements indicate that NiO$_x$ is the superior HTL. The highest effective lifetime of 1.1 µs among all HTLs indicates that once the charge carriers are extracted, they recombine the slowest for the samples with NiO$_x$. Correlating this result to the rate of bulk SRH recombination ($R_{\text{bulk-SRH}}$) in the perovskite with varying HTLs, we see that the $R_{\text{bulk-SRH}}$ is 2.5 to 3 orders of magnitude smaller for the perovskite with NiO$_x$ as an HTL than for the other three HTLs, explaining why NiO$_x$ enables the highest effective lifetime in the perovskite bulk among all four HTLs.

Summarizing all results, we can conclude that NiO$_x$ displays high absolute QFLS values because of a low trap density for the holes at the NiO$_x$–perovskite interface on the one hand and the long effective lifetime and low rate of trap-assisted recombination in the perovskite bulk on the other hand. However, the devices with NiO$_x$ also display the highest QFLS–V_{oc} offset among all four HTLs due to a prominent band misalignment at the NiO$_x$–perovskite interface, leading to a poor hole extraction, severe interfacial electron trapping, and thus, high interfacial SRH recombination. These findings are in line with the discussion in ref. 77, where the authors showed that the trapping of minority carriers (in this case, electrons at the NiO$_x$–perovskite interface) is directly proportional to a decrease in the devices' V_{oc}.

3.2. Influence of the recombination mechanisms on the stability of the solar cells

The good agreement between the simulated and experimentally-probed charge-carrier dynamics indicates that the here-discussed drift-diffusion simulations are trust-worthy within a reasonable error margin and can also be used to probe the stability and the degradation pathways in the cells. Thus, in this section we cross-compare the extracted parameters from the drift-diffusion simulations of the fresh and the aged solar cells and discuss the changes in the hole-trap density in the perovskite bulk or at the HTL–perovskite interface; all rates of recombination (direct, bulk SRH, and interface SRH); and all recombination current densities $J_{\text{Recombination}}$. As stated in the Methods section, SIMsalabim allows for a decomposition of the recombination types; at V_{oc}, $J_{\text{Recombination}}$ is calculated as the sum of all three individual recombination currents and equals J_{gen}.

Fig. 5 shows the results of MPP tracking of the solar cells with the four HTLs. NiO$_x$:Cu is the most stable HTL and maintains more than 92% of its initial PCE after two weeks of constant illumination and MPP tracking. The cells with NiO$_x$(:Cu) + SAM age in a comparable manner and maintain around 88–89% of their initial MPP. The cells with NiO$_x$ maintain around 85% of their initial efficiency.

First, we discuss the trap density of holes at the HTL–perovskite interface ($\text{Traps}_{\text{HTL-pero}}$) and in the perovskite bulk ($\text{Traps}_{\text{Bulk}}$) for both the fresh and the aged solar cells with varying HTLs (Fig. 6a).

Upon aging, NiO$_x$ exhibits a decrease in the hole-trap density at the HTL–perovskite interface by around a factor of ~3, but the density of bulk traps increases by a factor of ~36. For NiO$_x$:Cu, the interfacial trap density of holes remains almost unchanged in the fresh and in the old cells, while the density of the bulk traps almost triples. This could indicate a Cu migration in the perovskite bulk, but further investigation that goes beyond the scope of this article is needed to test this hypothesis. NiO$_x$ + SAM, similar to NiO$_x$, displays a decrease in the hole-trap density at the NiO$_x$ + SAM–perovskite interface; however, unlike NiO$_x$, the bulk trap density of the perovskite with NiO$_x$ + SAM as the underlying HTL does not change. For NiO$_x$:Cu + SAM, the aged cells display an increase by a factor of ~1.5 and ~9 in the hole-trap density at the HTL–perovskite interface and in the trap density in the bulk of the perovskite, respectively.

Next, we investigate the rates and current densities of recombination in the fresh and the aged solar cells. On the one hand, Fig. 6b presents all rates of recombination at V_{oc}: direct recombination (R_{bulk}), SRH recombination *via* bulk traps ($R_{bulk\text{-}SRH}$), and SRH recombination at the ETL–perovskite interface *via* interface (electron) traps ($R_{Int\text{-}SRH\text{-}n}$) or at the HTL–perovskite interface *via* holes ($R_{Int\text{-}SRH\text{-}p}$). On the other hand, Fig. 7 shows the recombination current densities as a function of the applied voltage, with the V_{oc} cross-over marked in blue, magenta, orange or black. When it comes to recombination current density for SRH recombination *via* interface traps, no distinction is made between the two interfaces; namely, the recombination current density is affected by the sum of the individual rates of recombination ($R_{Int\text{-}SRH\text{-}n}$ + $R_{Int\text{-}SRH\text{-}p}$).

By using Fig. 6 and 7 we can make several important observations.

First, the dominant recombination mechanism at V_{oc} for all cells, regardless of if they are fresh or aged, is the non-radiative SRH recombination *via* interface traps (pale purple lines in Fig. 7). It is roughly two to three orders of magnitude higher than the recombination rate for SRH recombination *via* bulk traps and around five orders of magnitude higher than direct recombination (Fig. 6b)). This finding is not surprising, as other studies point out that suppressing interfacial recombination in perovskite solar cells is still an ongoing issue.[11,76,78,80]

With respect to the recombination current densities at V_{oc} (Fig. 7), it can be seen that the radiative (=direct) recombination exhibits some minor changes after the aging. For instance, there is a slight increase in J_{direct} for NiO_x (Fig. 7a) and a slight decrease for NiO_x:Cu (Fig. 7d) from the fresh to the aged cell, but since direct recombination is not the dominant recombination mechanism in the cells, these effects are neglected. Therefore, the following discussion centers around the bulk and the interface SRH recombination.

As seen in Fig. 6b, the fresh cells with NiO_x have a more than two orders of magnitude higher rate of SRH interfacial recombination at their ETL–perovskite interface ($R_{Int\text{-}SRH\text{-}n}$), likely due to trapping of electrons, compared to the other three HTLs, indicating that a sub-optimal HTL affects the ETL–perovskite interface as well. NiO_x:Cu significantly decreases the electron trapping at the HTL–perovskite interface, and SAM halves the trapping of electrons of NiO_x:Cu. The rate of SRH interfacial recombination due to trapping of holes ($R_{Int\text{-}SRH\text{-}p}$) is the lowest for NiO_x, then for NiO_x + SAM, while NiO_x:Cu and NiO_x:Cu +AM display almost identical $R_{Int\text{-}SRH\text{-}p}$.

For the aged cells, the most prominent change is displayed in NiO_x + SAM, whose rate of SRH recombination at V_{oc} at the ETL–perovskite interface due to electron trapping ($R_{Int\text{-}SRH\text{-}n}$) increases by a factor of ~88. However, this increase is also accompanied by a decrease of two orders of magnitude in the rate of non-radiative recombination due to hole trapping at the HTL–perovskite interface ($R_{Int\text{-}SRH\text{-}p}$), eventually yielding an almost unchanged overall rate of interface SRH recombination ($J_{interface\text{-}SRH}$) at V_{oc} (see Fig. 7b).

The aged cells with NiO_x display an increase by a factor of ~1.3 in the rate of non-radiative SRH recombination at the ETL–perovskite interface due to electron trapping ($R_{Int\text{-}SRH\text{-}n}$), but this effect is suppressed by the decrease by a factor of ~2 in the rate of interfacial recombination due to trapping of holes ($R_{Int\text{-}SRH\text{-}p}$). Therefore, similarly to NiO_x + SAM, the overall rate of interface SRH recombination ($J_{interface\text{-}SRH}$) at V_{oc} does not change much for the fresh and the aged cells (Fig. 7a). By analogy, the same conclusions can be made for NiO_x:Cu (+SAM) and it can be concluded that the interface SRH recombination current density does not change significantly in the fresh and in the aged cells, even if the individual trapping of either the holes or the electrons might change.

However, unlike the direct and trap-assisted (SRH) interface recombination, which stay approximately constant, the SRH recombination in the bulk of the perovskite increases in all cells as they age. The cells with NiO_x display an order of magnitude higher trap-assisted recombination in the perovskite bulk, which can be explained by the significant increase in the trap density in the perovskite bulk (see the $Traps_{bulk}$ bar for NiO_x in Fig. 6a). A similar effect is present in the cells with NiO_x:Cu, NiO_x + SAM, and NiO_x:Cu + SAM. The increase in the bulk trap-assisted recombination is the lowest for the cells with NiO_x:Cu, while for NiO_x + SAM and NiO_x:Cu + SAM the final bulk trap-assisted recombination is similar.

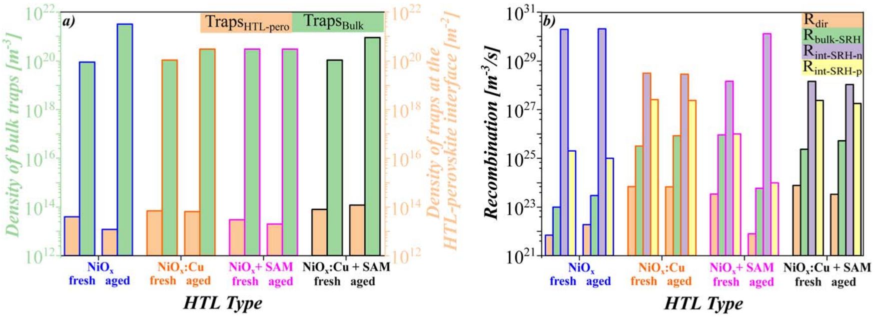

Fig. 6 (a) Hole trap density at the HTL–perovskite interface ($Traps_{HTL\text{-}pero}$) and in the perovskite bulk ($Traps_{Bulk}$), followed by (b) varying rates of recombination at V_{oc} for fresh and aged single-junction perovskite solar cells with NiO_x(:Cu) (+SAM) HTLs and C_{60}–SnO_2 as the ETL stack. R_{dir}: direct recombination; $R_{bulk\text{-}SRH}$: recombination *via* bulk traps; $R_{Int\text{-}SRH\text{-}n}$ or $R_{Int\text{-}SRH\text{-}p}$: recombination *via* interface traps, where n and p distinguish between trapping of electrons and holes at the ETL– and HTL–perovskite interfaces, respectively. The frames around the bars follow the same color coding as the HTLs.

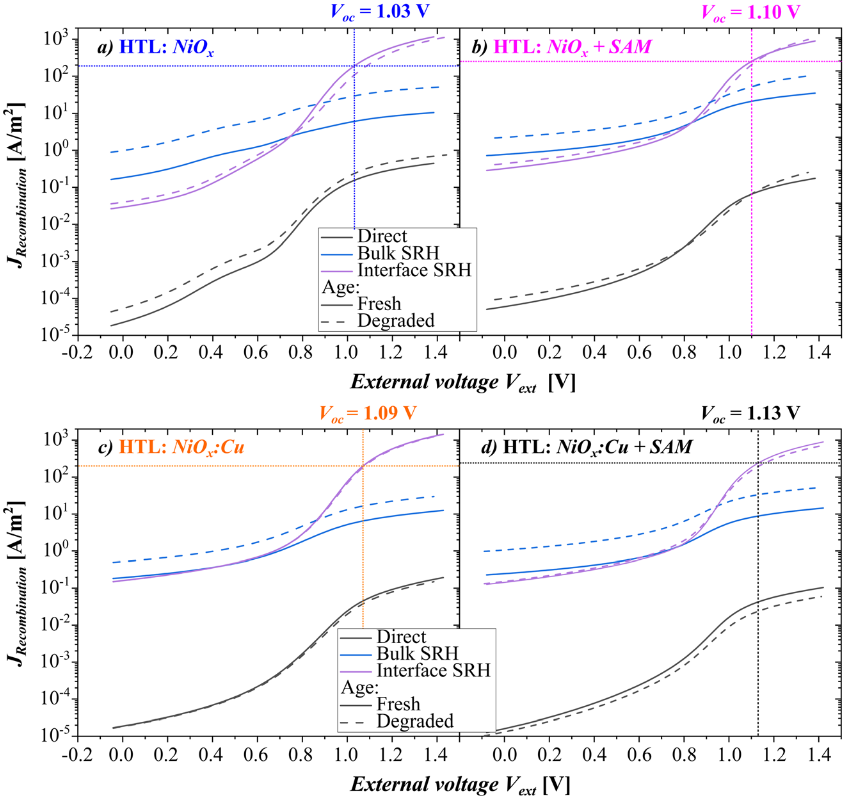

Fig. 7 Overall direct, bulk SRH, and interface SRH recombination current densities in fresh (solid lines) and aged (dashed lines) p-i-n single-junction perovskite solar cells with NiO_x(:Cu) (+SAM) HTLs and C_{60}–SnO_2 as the ETL stack.

As determined in the aged cells, these simulations reveal that the degradation of the cells is directly proportional to the increase in the trap-assisted recombination in the perovskite bulk. This correlation is seen for all samples, out of which the perovskite deposited on top of NiO_x degrades the strongest and has the most prominent increase in the bulk trap-assisted recombination. Opposite to the cells with NiO_x, for the perovskite deposited on top of NiO_x:Cu, the minimum degradation is observed. Therefore, it can be concluded that even though the interface SRH remains the dominant recombination mechanism, the main cause for the degradation of the solar cells is the increased rate of SRH recombination in the perovskite bulk, which additionally can be influenced by the underlying HTL. Furthermore, Clarke *et al.* have also recently shown that an increase in the recombination rate in the perovskite bulk can be contributed to a rise in the densities of ion vacancies and/or mobile ions.[16]

3.3. Mobile ions and hysteresis in the *JV* curves

This section looks into (1) the HF at varying scan speeds, and (2) the connection of the HF at a scanning speed of 0.5 V s^{-1} to the total ion density. The results are summarized in Fig. 8 and in Table 1, while all the *JV* curves at the varying scan speeds can be found in the SI.

The steady-state drift-diffusion allowed both positive and negative ionic species to be mobile. As already mentioned in the Methods section, allowing either positive or negative ions to move was also tested, but such specifications caused a mismatch between the simulated and the measured R_{sh}. Allowing for both types of ions to move when NiO_x is the HTL is not so unreasonable. On one hand, I^- and Br^- are often assigned as the dominant mobile ion species[81,82] in the perovskite. On the other hand, recent studies show that proton diffusion might also be relevant.[83] On the HTL side, it has been shown that the positively-charged Ni^{3+} defects in the NiO_x can lead to chemical reactions at the NiO_x–perovskite interface and cause more prominent I^- or Br^- migration.[8] For NiO_x:Cu, additionally, Cu^{2+} ions could also be potentially mobile, creating traps in the perovskite bulk, as already mentioned when discussing Fig. 6b.

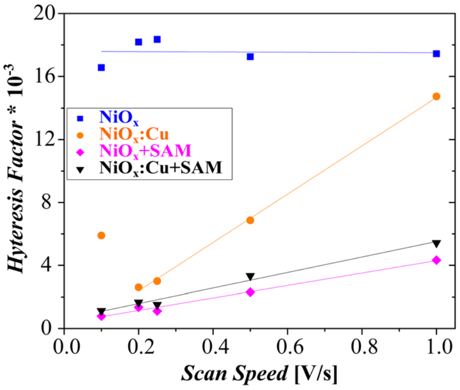

Fig. 8 Hysteresis factor (HF) as a function of the scan speed [V s^{-1}] during the *JV* measurements.

Table 1 Concentration of negative (n_{ion}) and positive (p_{ion}) ions and their total number (total$_{ion}$), which is conserved during the simulation. The values were extracted by simulating the *JV* measurements performed at 0.5 V s^{-1}

HTL	n_{ion}	p_{ion} [$\times 10^{21}$ m^{-3}]	Total$_{ion}$
NiO_x	15.77	1.47	17.21
NiO_x:Cu	0.57	9.35	9.92
NiO_x + SAM	0.37	2.47	2.85
NiO_x:Cu + SAM	0.11	6.21	6.32

In principle, all cells have a rather small hysteresis factor (HF) on the order of 10^{-3} (Fig. 8). However, a low HF does not directly translate to (almost) no ionic movement, since both the scan speed and the amount of non-radiative combination will influence the HF, implying that HF can vary if there is a change in one or several of the following factors:[66] the location or amount of non-radiative recombination; the concentration of ions; and the transients of the ions (to be probed with time-resolved simulations). Additionally, it is possible that with the scan speeds in the range of 0.1 V s^{-1} to 1 V s^{-1}, the region of enhanced hysteresis has not yet been probed, as other studies show a peak in the hysteresis at scan speeds of around 10 V s^{-1}.[66] Finally, Thiesbrummel *et al.* have shown that even for seemingly hysteresis-free cells, the role of mobile ions cannot be neglected.[84]

Fig. 8 and Table 1 indicate that NiO_x has the highest hysteresis factor (~18 × 10^{-3}) and the highest total ion concentration, out of which the dominant species are the negative ions. This also connects to an increased trap-assisted recombination due to a high trapping and accumulation of electrons (Fig. 6b).

Some studies show that NiO_x enhances the movement of the I^- ions, resulting in chemical reactions at the NiO_x–perovskite interface[8] and resulting in a phase segregation in the perovskite.[85] The correlation between ionic movement in the perovskite bulk, charge trapping at the NiO_x–perovskite interface, and the chemical reactions between the ions from the perovskite with the Ni^{3+} defects in the NiO_x would then, as indicated by these simulations, increase the trap-assisted recombination in the bulk of the perovskite, eventually resulting in degradation of the solar cell.

In addition to phase segregation, the traps in the perovskite bulk might also be caused by intrinsic point defects/vacancies in the perovskite crystal lattice; grain boundaries, which are often regarded as cracks in the perovskite crystal lattice;[86–88] or even impurities that act as recombination hot spots.[89] However, all of these defects not only influence the bulk of the perovskite, but also the interfaces, as first-principle calculations have indicated that these defects are leaving the bulk and moving towards the transport-layer interfaces.[86–88] Therefore, the devices with NiO_x – which display severe trapping of electrons at the NiO_x–perovskite interface, a higher ion density, and an increased bulk-trap density and bulk trap-assisted recombination as they age – might suffer from a combination of the above-mentioned defects. To truly disentangle all of them and assign a dominant defect, further characterization, which goes beyond the scope of this study, is needed.

NiO_x:Cu has a similar HF at a scan speed of 0.2 V s^{-1} to NiO_x(:Cu) + SAM, but with increased scan speed, the HF grows linearly. At 0.5 V s^{-1}, the HF is ~6 × 10^{-3}, indicating that there might be an enhanced ion migration in these cells at moderate scan rates. The ions are likely to be positive Cu^{2+} ions migrating into the perovskite bulk, since Table 1 indicates a positive-ion concentration of ~ 9 × 10^{21} m^{-3}, which is then decreased (~6 × 10^{21} m^{-3}) by the SAM surface passivation.

NiO_x + SAM and NiO_x:Cu + SAM exhibit an almost identical slope for their increase in the HF, which remains lower than the HF of the samples with NiO_x(:Cu) even at higher scan rates. This finding indicates that SAM passivates the NiO_x(:Cu) and suppresses the ion migration from the HTL into the perovskite bulk and consecutively decreases the recombination rate of bulk trap-assisted recombination.

However, it is intriguing to see that even though at a scan speed of 0.5 V s^{-1} NiO_x:Cu has a higher HF and a higher total ion concentration than NiO_x(:Cu) + SAM, the rates of recombination in the fresh cells with these three HTLs (Fig. 6b, fresh) and their total recombination current densities (Fig. 7) are comparable. Additionally, with respect to the stability (Fig. 5), NiO_x:Cu is the most stable HTL, which is counter-intuitive when seeing the ion concentration and the prominent ionic movement implied by the strong dependence of the HF on the scan speed. It could be that the migrating positive ions have a more pronounced effect on the solar-cell stability only at higher scan speeds and/or at elevated temperatures – both of which are investigations that go beyond the scope of this study. Finally, even though here the trends in the stability of the devices are explored as a function of the HTL, the stability of the solar cell is also influenced by the individual stability of the SAM, the perovskite bulk, and the ETL, as well as the interplay between these layers.

4. Conclusion

This research uniquely investigated the stability of tandem-compatible, wide-bandgap perovskite solar cells using low-temperature magnetron sputtered NiO_x that is bulk doped with Cu and/or surface passivated with MeO-2PACz SAM. The operational stability was tested *via* continuous maximum power point (MPP) tracking, but more importantly, it was also evaluated *via* a 1D drift-diffusion simulation that incorporates the role of mobile ions. A unique aspect of this study is the simulation of both fresh and aged devices, allowing direct insight into degradation mechanisms over time.

These simulations represent a fine balance between carefully choosing which parameters to fine-tune while keeping constant as many experimentally-measured input parameters as possible. The certainty in grasping the underlying device physics *via* these simulations is strengthened by the successful reproduction of experimentally-obtained results (QLFS–V_{oc} offsets, TrPL, tr-SPV, and UPS measurements), as constraining a large number of the input parameters resulted in an excellent agreement of the simulated results with the experimental measurements and former literature findings. Thus, the results indicate that the drift-diffusion model is describing the underlying device physics and capturing the limiting factors at the HTL–perovskite interface very successfully.

The results were structured around three aspects of the cells: (1) the band alignment, (2) the difference in the recombination mechanisms between the fresh and the aged cells, and (3) the interplay between the ion density, hysteresis, and stability of the solar cells.

The simulations were especially insightful to pin-point the key short comings of the low-temperature sputtered NiO_x. We find that the cells with NiO_x have the most unfavorable band alignment, leading to a non-negligible QFLS–V_{oc} offset. In agreement with the TrPL measurements, the drift-diffusion simulations also indicate that the cells with NiO_x display prominent trapping of electrons, resulting in an increased rate of interfacial SRH recombination, especially at the ETL–perovskite interface. The excess of charge carriers could possibly be promoted by the ion density or ion movement in the perovskite bulk when NiO_x is used as an HTL, eventually degrading the perovskite bulk and negatively affecting the cells' stability. This hypothesis is also supported by the simulated ion density for the cell with NiO_x, which shows the highest value among all four-investigated HTLs, along with the most pronounced hysteresis and most prominent degradation. The performance and the stability of the cells can be improved with both the bulk doping and the surface passivation, mostly because of improved interface charge-carrier dynamics and lower ion density.

Finally, on a broader level, we point out that simulating both fresh and aged *JV* curves can provide fundamental insights for the degradation pathways in the cells. As such, we advocate for adoption of this methodology by the scientific community so that we can jointly boost the devices' stability and prepare them for commercialization.

Conflicts of interest

There authors declare neither conflicts of interests nor competing financial interests.

Data availability

The raw data that supports the plots within this paper and other findings of this study are available from the corresponding authors upon reasonable request.

Supplementary information (SI) is available. See DOI: https://doi.org/10.1039/d5se00474h.

Acknowledgements

Ivona Kafedjiska is grateful for the funding that was provided by the Helmholtz Association within the project HySPRINT Innovation Lab and by the Federal Ministry of Economoy and Energy (Bundesministerium für Wirtschaft und Energie) for the speedCIGS project (Grant No. 0324095D). Vincent M. Le Corre acknowledges support from the Villum Foundation, Grant No. 50440. Ivona Kafedjiska would also like to thank A. Steigert and R. Wenisch for technical support for the development of the NiO_x sputtering process, H. Hempel for the TrPL measurements, C. A. Kaufmann for discussing the results, and S. Albrecht and A. Abate for access to the HySPRINT Innovation Lab infrastructure.

References

1 *Best Research-Cell Efficiency Chart*, url: https://www.nrel.gov/pv/cell-efficiency.html, visited on 12/20/2021.
2 N. Ahn and M. Choi, Towards Long-Term Stable Perovskite Solar Cells: Degradation Mechanisms and Stabilization Techniques, *Advanced Science*, 2024, **11**(4), 2306110.
3 J. Wen, *et al.*, Heterojunction formed *via* 3D-to-2D perovskite conversion for photostable wide-bandgap perovskite solar cells, *Nat. Commun.*, 2023, **14**(1), 7118.
4 Q. Jiang, *et al.*, Surface passivation of perovskite film for efficient solar cells, *Nat. Photonics*, 2019, **13**(7), 460–466.
5 J. Jeong, *et al.*, Pseudo-halide anion engineering for α-FAPbI3 perovskite solar cells, *Nature*, 2021, **592**, 381–385.
6 B.-B. Yu, *et al.*, Heterogeneous 2D/3D tin-halides perovskite solar cells with certified conversion efficiency breaking 14, *Adv. Mater.*, 2021, **33**(36), 2102055.
7 E. Aydin, M. De Bastiani and S. De Wolf, Defect and Contact Passivation for Perovskite Solar Cells, *Adv. Mater.*, 2019, **31**, 1900428, DOI: 10.1002/adma.201900428.
8 C. C. Boyd, *et al.*, Overcoming Redox Reactions at Perovskite-Nickel Oxide Interfaces to Boost Voltages in Perovskite Solar Cells, *Joule*, 2020, **4**(8), 1759–1775, DOI: 10.1016/j.joule.2020.06.004.
9 S. Ito, *et al.*, Effects of surface blocking layer of Sb_2S_3 on nanocrystalline TiO_2 for $CH_3NH_3PbI_3$ perovskite solar cells, *J. Phys. Chem. C*, 2014, **118**, 16995–17000, DOI: 10.1021/jp500449z.
10 S. N. Habisreutinger, *et al.*, Dopant-free planar n-i-p perovskite solar cells with steady-state efficiencies exceeding 18, *ACS Energy Lett.*, 2017, **2**, 622–628, DOI: 10.1021/acsenergylett.7b00028.
11 C. M. Wolff, *et al.*, Reduced Interface-Mediated Recombination for High Open-Circuit Voltages in $CH_3NH_3PbI_3$ Solar Cells, *Adv. Mater.*, 2017, **29**, 1700159, DOI: 10.1002/adma.201700159.
12 P. Calado, *et al.*, Evidence for ion migration in hybrid perovskite solar cells with minimal hysteresis, *Nat. Commun.*, 2016, **7**(1), 13831, DOI: 10.1038/ncomms13831.
13 N. E. Courtier, *et al.*, How transport layer properties affect perovskite solar cell performance: insights from a coupled charge transport/ion migration model, *Energy Environ. Sci.*, 2019, **12**(1), 396–409, DOI: 10.1039/C8EE01576G.
14 V. M. Le Corre, *et al.*, Quantification of Efficiency Losses Due to Mobile Ions in Perovskite Solar Cells *via* Fast Hysteresis Measurements, *Sol. RRL*, 2022, **6**(4), 2100772, DOI: 10.1002/solr.202100772.
15 J. Thiesbrummel, *et al.*, Ion-induced field screening as a dominant factor in perovskite solar cell operational stability, *Nat. Energy*, 2024, **9**(6), 664–676.
16 W. Clarke, P. Cameron and G. Richardson, Predicting Long-Term Stability from Short-Term Measurement: Insights from

Modeling Degradation in Perovskite Solar Cells during Voltage Scans and Impedance Spectroscopy, *J. Phys. Chem. Lett.*, 2024, **15**(47), 11730–11736.

17 L. J. F. Hart, *et al.*, More is different: mobile ions improve the design tolerances of perovskite solar cells, *Energy Environ. Sci.*, 2024, **17**, 7107–7118.

18 I. Kafedjiska, *et al.*, Advanced Characterization and Optimization of NiO_x: Cu-SAM Hole-Transporting Bi-Layer for 23.4% Efficient Monolithic Cu (In, Ga) Se_2-Perovskite Tandem Solar Cells, *Adv. Funct. Mater.*, 2023, **33**, 2302924.

19 K. Wojciechowski, *et al.*, C_{60} as an Efficient n-Type Compact Layer in Perovskite Solar Cells, *J. Phys. Chem. Lett.*, 2015, **6**(12), 2399–2405, DOI: 10.1021/acs.jpclett.5b00902.

20 J.-P. Correa-Baena, *et al.*, Identifying and suppressing interfacial recombination to achieve high open-circuit voltage in perovskite solar cells, *Energy Environ. Sci.*, 2017, **10**(5), 1207–1212, DOI: 10.1039/c7ee00421d.

21 D. Bryant, *et al.*, Observable Hysteresis at Low Temperature in 'Hysteresis Free' Organic–Inorganic Lead Halide Perovskite Solar Cells, *J. Phys. Chem. Lett.*, 2015, **6**(16), 3190–3194, DOI: 10.1021/acs.jpclett.5b01381.

22 I. Levine, *et al.*, Interface-Dependent Ion Migration/Accumulation Controls Hysteresis in $MAPbI_3$ Solar Cells, *J. Phys. Chem. C*, 2016, **120**(30), 16399–16411, DOI: 10.1021/acs.jpcc.6b04233.

23 B. Roose, Q. Wang and A. Abate, The Role of Charge Selective Contacts in Perovskite Solar Cell Stability, *Adv. Energy Mater.*, 2019, **9**(5), 1803140, DOI: 10.1002/aenm.201803140.

24 A. Al-Ashouri, *et al.*, Monolithic perovskite/silicon tandem solar cell with¿ 29% efficiency by enhanced hole extraction, *Science*, 2020, **370**, 1300–1309, DOI: 10.1126/science.abd4016.

25 I. Kafedjiska, *et al.*, Disentangling the effect of the hole-transporting layer, the bottom, and the top device on the fill factor in monolithic CIGSe-Perovskite tandem solar cells by using spectroscopic and imaging tools, *J. Phys.: Energy*, 2023, **5**, 024014, DOI: 10.1088/2515-7655/acc277.

26 I. Kafedjiska, *et al.*, Integration of rough RTP absorbers into CIGS-perovskite monolithic tandems by NiO_x(:Cu)+ SAM Hole-transporting Bi-layers, *Sol. Energy Mater. Sol. Cells*, 2023, **254**, 112248, DOI: 10.1016/j.solmat.2023.112248.

27 E. Aydin, *et al.*, Enhanced optoelectronic coupling for perovskite-silicon tandem solar cells, *Nature*, 2023, 732–738, DOI: 10.1038/s41586-023-06667-4.

28 D. Di Girolamo, *et al.*, Progress, highlights and perspectives on NiO in perovskite photovoltaics, *Chem. Sci.*, 2020, **11**(30), 7746–7759, DOI: 10.1039/D0SC02859B.

29 T. Abzieher, *et al.*, Electron-Beam-Evaporated Nickel Oxide Hole Transport Layers for Perovskite-Based Photovoltaics, *Adv. Energy Mater.*, 2019, **9**(12), 1802995, DOI: 10.1002/aenm.201802995.

30 D. Koushik, *et al.*, Plasma-assisted atomic layer deposition of nickel oxide as hole transport layer for hybrid perovskite solar cells, *J. Mater. Chem. C*, 2019, **7**(40), 12532–12543, DOI: 10.1039/C9TC04282B.

31 H. Lee, *et al.*, Engineered optical and electrical performance of rf–sputtered undoped nickel oxide thin films for inverted perovskite solar cells, *Sci. Rep.*, 2018, **8**(1), 5590, DOI: 10.1038/s41598-018-23907-0.

32 Y. Zhang, *et al.*, Modulation of Ni^{3+} and crystallization of dopant-free NiO_x hole transporting layer for efficient p-i-n perovskite solar cells, *Electrochim. Acta*, 2019, **319**, 41–48, DOI: 10.1016/j.electacta.2019.06.168.

33 E. Aydin, *et al.*, Room-Temperature-Sputtered Nanocrystalline Nickel Oxide as Hole Transport Layer for p-i-n Perovskite Solar Cells, *ACS Appl. Energy Mater.*, 2018, **1**(11), 6227–6233, DOI: 10.1021/acsaem.8b01263.

34 E. L. Ratcliff, *et al.*, Evidence for near-Surface NiOOH Species in Solution-Processed NiO_x Selective Interlayer Materials: Impact on Energetics and the Performance of Polymer Bulk Heterojunction Photovoltaics, *Chem. Mater.*, 2011, **23**(22), 4988–5000, DOI: 10.1021/cm202296p.

35 C. M. Lin and C. C. Wu, Effect of the Ni^{2+}/Ni^{3+} Concentration on the Optoelectronical Properties of Lithium-Doped Nickel Oxide Films, *ACS Appl. Electron. Mater.*, 2021, **3**, 1050–1057, DOI: 10.1021/acsaelm.0c00752.

36 M. Yan, *et al.*, Room-temperature Sputtered NiO_x for hysteresis-free and stable inverted Cs-FA mixed-cation perovskite solar cells, *Mater. Sci. Semicond. Process.*, 2020, **115**, 105129, DOI: 10.1016/j.mssp.2020.105129.

37 J. D. Hwang and T. H. Ho, Effects of oxygen content on the structural, optical, and electrical properties of NiO films fabricated by radio-frequency magnetron sputtering, *Mater. Sci. Semicond. Process.*, 2017, **71**, 396–400, DOI: 10.1016/j.mssp.2017.09.002.

38 Md. Bodiul Islam, *et al.*, NiO_x Hole Transport Layer for Perovskite Solar Cells with Improved Stability and Reproducibility, *ACS Omega*, 2017, **2**, 2291–2299, DOI: 10.1021/acsomega.7b00538.

39 J. Keraudy, *et al.*, Process- and optoelectronic-control of NiO_x thin films deposited by reactive high power impulse magnetron sputtering, *J. Appl. Phys.*, 2017, **121**(17), 171916, DOI: 10.1063/1.4978349.

40 G. Li, *et al.*, Overcoming the Limitations of Sputtered Nickel Oxide for High-Efficiency and Large-Area Perovskite Solar Cells, *Advanced Science*, 2017, **4**(12), 1700463, DOI: 10.1002/advs.201700463.

41 N. Pant, *et al.*, Effect of different surface treatments of sputtered NiO X on the photovoltaic parameters of perovskite solar cells: a correlation study, *Appl. Phys. Express*, 2020, **13**(2), 025505, DOI: 10.35848/1882-0786/ab6bde.

42 M.-A. Park, *et al.*, Enhanced electrical properties of Li–doped NiO_x hole extraction layer in p-i-n type perovskite solar cells, *Curr. Appl. Phys.*, 2017, **18**, S55–S59, DOI: 10.1016/j.cap.2017.11.010.

43 Y. Xie, *et al.*, Enhancing Photovoltaic Performance of Inverted Planar Perovskite Solar Cells by Cobalt-Doped Nickel Oxide Hole Transport Layer, *ACS Appl. Mater. Interfaces*, 2018, **10**, 14153–14159, DOI: 10.1021/acsami.8b01683.

44 R. Kaneko, *et al.*, Cobalt-doped nickel oxide nanoparticles as efficient hole transport materials for low-temperature

processed perovskite solar cells, *Sol. Energy*, 2019, **181**, 243–250, DOI: 10.1016/j.solener.2019.01.097.

45 F. P. G. Choi, *et al.*, First demonstration of lithium, cobalt and magnesium introduced nickel oxide hole transporters for inverted methylammonium lead triiodide based perovskite solar cells, *Sol. Energy*, 2021, **215**, 434–442, DOI: 10.1016/j.solener.2020.12.068.

46 M. Feng, *et al.*, High-Efficiency and Stable Inverted Planar Perovskite Solar Cells with Pulsed Laser Deposited Cu-Doped NiO_x Hole-Transport Layers, *ACS Appl. Mater. Interfaces*, 2020, **12**(45), 50684–50691, DOI: 10.1021/acsami.0c15923.

47 S. Zhumagali, *et al.*, Linked Nickel Oxide/Perovskite Interface Passivation for High-Performance Textured Monolithic Tandem Solar Cells, *Adv. Energy Mater.*, 2021, **11**(40), 2101662, DOI: 10.1002/aenm.202101662.

48 N. Phung, *et al.*, Enhanced Self-Assembled Monolayer Surface Coverage by ALD NiO in p-i-n Perovskite Solar Cells, *ACS Appl. Mater. Interfaces*, 2022, **14**(1), 2166–2176, DOI: 10.1021/acsami.1c15860.

49 R. Pengbin, *et al.*, High Electron Affinity Enables Fast Hole Extraction for Efficient Flexible Inverted Perovskite Solar Cells, *Adv. Energy Mater.*, 2020, **10**, 1903487, DOI: 10.1002/aenm.201903487.

50 Y. Li, *et al.*, Recent progress of critical interface engineering for highly efficient and stable perovskite solar cells, *Adv. Energy Mater.*, 2022, **12**(5), 2102730.

51 G. Ma, *et al.*, Magnetron sputtered nickel oxide with suppressed interfacial defect states for efficient inverted perovskite solar cells, *J. Energy Chem.*, 2025, **100**, 348–355.

52 L. Zheng, *et al.*, Surface Property Regulation of a Magnetron-Sputtered NiO_x Hole Transport Layer for High-Performance Inverted Perovskite Solar Cells, *ACS Appl. Mater. Interfaces*, 2024, **16**(40), 54272–54281.

53 X. Liu, *et al.*, Optimizing the Performance of Sputtered-NiO_x-Based Perovskite Solar Cells *via* Regulating the PbI2 Concentration, *Energy Technol.*, 2023, **11**, 2300355.

54 O. Almora, *et al.*, Instability analysis of perovskite solar cells *via* short-circuit impedance spectroscopy: A case study on NiO_x passivation, *J. Appl. Phys.*, 2024, **136**, 9.

55 J. Mohanraj, *et al.*, NiO_x passivation in perovskite solar cells: from surface reactivity to device performance, *ACS Appl. Mater. Interfaces*, 2024, **16**(32), 42835–42850.

56 Y. Yang, *et al.*, Inverted perovskite solar cells with over 2000 h operational stability at 85 °C using fixed charge passivation, *Nat. Energy*, 2024, **9**(1), 37–46.

57 Y. Zhou, *et al.*, Interfacial modification of NiO_x for highly efficient and stable inverted perovskite solar cells, *Adv. Energy Mater.*, 2024, **14**(25), 2400616.

58 B. Sharma, *et al.*, Buried Interfacial Passivation in NiO_x-Based Inverted Semi-Transparent Perovskite Solar Cells, *Small*, 2025, 2502654.

59 L. Cao, *et al.*, Modification of Nickel Oxide *via* Self-Assembled Monolayer for Enhanced Performance of Air-Processed FAPbl3 Perovskite Solar Cells, *ACS Appl. Energy Mater.*, 2024, **7**(4), 1508–1516.

60 L. Lin, *et al.*, Thermally-stable and highly-efficient bi-layered NiO_x-based inverted planar perovskite solar cells by employing a p-type organic semiconductor, *Chem. Eng. J.*, 2022, **443**, 136405.

61 J. Yang, *et al.*, Overcome low intrinsic conductivity of NiO_x through triazinyl modification for highly efficient and stable inverted perovskite solar cells, *Sol. RRL*, 2022, **6**(9), 2200422.

62 M. Koopmans, V. M. Le Corre and L. Jan Anton Koster, SIMsalabim‘: An open-source drift-diffusion simulator for semiconductor devices, *J. Open Source Softw.*, 2022, **7**(70), 3727, DOI: 10.21105/joss.03727.

63 Koster Group, *SIMsalabim Project*, 2022, url: https://github.com/kostergroup/SIMsalabim, visited on 05/23/2022.

64 M. Burgelman, P. Nollet and S. Degrave, Modelling polycrystalline semiconductor solar cells, *Thin Solid Films*, 2000, 361–362, DOI: 10.1016/S0040-6090(99)00825-1.

65 *Simulation Programme SCAPS-1D for Thin Film Solar Cells*, url: https://scaps.elis.ugent.be/, visited on 05/23/2022.

66 V. M. Le Corre *et al.*, Device Modeling of Perovskite Solar Cells: Insights and Outlooks, *Soft-Matter Thin Film Solar Cells*, AIP Publishing Books. AIP Publishing LLC, 2020, pp. 4–32, DOI: 10.1063/9780735422414_004.

67 P. Calado, *et al.*, Driftfusion: an open source code for simulating ordered semiconductor devices with mixed ionic-electronic conducting materials in one dimension, *J. Comput. Electron.*, 2022, **21**(4), 960–991.

68 N. E. Courtier, *et al.*, Ionmonger: a free and fast planar perovskite solar cell simulator with coupled ion vacancy and charge carrier dynamics, *J. Comput. Electron.*, 2019, **18**(4), 1435–1449.

69 W. Clarke, *et al.*, IonMonger 2.0: software for free, fast and versatile simulation of current, voltageand impedance response of planar perovskite solar cells, *J. Comput. Electron.*, 2023, **22**, 364–382.

70 M. Saliba, *et al.*, Cesium-containing triple cation perovskite solar cells: improved stability, reproducibility and high efficiency, *Energy Environ. Sci.*, 2016, **9**(6), 1989–1997, DOI: 10.1039/C5EE03874J.

71 H. Köbler, *et al.*, High-Throughput Aging System for Parallel Maximum Power Point Tracking of Perovskite Solar Cells, *Energy Technol.*, **10**(6), 2200234, DOI: 10.1002/ente.202200234.

72 M. T. Neukom, *et al.*, Why perovskite solar cells with high efficiency show small IV-curve hysteresis, *Sol. Energy Mater. Sol. Cells*, 2017, **169**, 159–166, DOI: 10.1016/j.solmat.2017.05.021.

73 T. S. Sherkar, *et al.*, Recombination in Perovskite Solar Cells: Significance of Grain Boundaries, Interface Traps, and Defect Ions, *ACS Energy Lett.*, 2017, **2**(5), 1214–1222, DOI: 10.1021/acsenergylett.7b00236.

74 T. Nir and Y. Vaynzof, Preventing Hysteresis in Perovskite Solar Cells by Undoped Charge Blocking Layers, *ACS Appl. Energy Mater.*, 2018, **1**(2), 676–683, DOI: 10.1021/acsaem.7b00176.

75 P. Caprioglio, *et al.*, On the Relation between the Open-Circuit Voltage and Quasi-Fermi Level Splitting in Efficient

Perovskite Solar Cells, *Adv. Energy Mater.*, 2019, **9**, 1901631, DOI: 10.1002/aenm.201901631.

76 M. Stolterfoht, *et al.*, The impact of energy alignment and interfacial recombination on the internal and external open-circuit voltage of perovskite solar cells, *Energy Environ. Sci.*, 2019, **12**(9), 2778–2788, DOI: 10.1039/C9EE02020A.

77 M. Koopmans and L. J. Anton Koster, Voltage deficit in wide bandgap perovskite solar cells: the role of traps, band energies, and effective density of states, *Sol. RRL*, 2022, **6**, 2200560.

78 C. M. Wolff, *et al.*, Nonradiative Recombination in Perovskite Solar Cells: The Role of Interfaces, *Adv. Mater.*, 2019, **31**(52), 1902762, DOI: 10.1002/adma.201902762.

79 I. Levine, *et al.*, Charge transfer rates and electron trapping at buried interfaces of perovskite solar cells, *Joule*, 2021, **5**, 2915–2933, DOI: 10.1016/j.joule.2021.07.016.

80 M. Stolterfoht, *et al.*, Visualization and suppression of interfacial recombination for high-efficiency large-area pin perovskite solar cells, *Nat. Energy*, 2018, **3**(10), 847–854, DOI: 10.1038/s41560-018-0219-8.

81 T. Zhang, C. Hu and S. Yang, Ion Migration: A 'Double-Edged Sword' for Halide-Perovskite-Based Electronic Devices, *Small Methods*, 2020, **4**(5), 1900552, DOI: 10.1002/smtd.201900552.

82 E. Mosconi and F. De Angelis, Mobile Ions in Organohalide Perovskites: Interplay of Electronic Structure and Dynamics, *ACS Energy Lett.*, 2016, **1**(1), 182–188, DOI: 10.1021/acsenergylett.6b00108.

83 D. R. Ceratti, *et al.*, Eppur si Muove: Proton Diffusion in Halide Perovskite Single Crystals, *Adv. Mater.*, 2020, **32**(46), 2002467, DOI: 10.1002/adma.202002467.

84 J. Thiesbrummel, *et al.*, Universal current losses in perovskite solar cells due to mobile ions, *Adv. Energy Mater.*, 2021, **11**(34), 2101447.

85 Y. Lin, *et al.*, Excess charge-carrier induced instability of hybrid perovskites, *Nat. Commun.*, 2018, **9**(1), 4981, DOI: 10.1038/s41467-018-07438-w.

86 A. Buin, *et al.*, Halide-Dependent Electronic Structure of Organolead Perovskite Materials, *Chem. Mater.*, 2015, **27**(12), 4405–4412, DOI: 10.1021/acs.chemmater.5b01909.

87 C. Eames, *et al.*, Ionic transport in hybrid lead iodide perovskite solar cells, *Nat. Commun.*, 2015, **6**(1), 7497, DOI: 10.1038/ncomms8497.

88 P. Delugas, *et al.*, Thermally Activated Point Defect Diffusion in Methylammonium Lead Trihalide: Anisotropic and Ultrahigh Mobility of Iodine, *J. Phys. Chem. Lett.*, 2016, **7**(13), 2356–2361, DOI: 10.1021/acs.jpclett.6b00963.

89 M. Yavari, *et al.*, How far does the defect tolerance of lead-halide perovskites range? The example of Bi impurities introducing efficient recombination centers, *J. Mater. Chem. A*, 2019, **7**(41), 23838–23853, DOI: 10.1039/C9TA01744E.